Mediterranean Geoscience Reviews (2022) 4:471–494
https://doi.org/10.1007/s42990-022-00090-z

ORIGINAL PAPER

Reassessing the rupture process of the 2003 Boumerdes-Zemmouri earthquake (Mw 6.8, northern Algeria) using teleseismic, strong motion, InSAR, GPS, and coastal uplift data

Hamoud Beldjoudi[1] · **Bertrand Delouis**[2]

Received: 7 July 2022 / Revised: 21 August 2022 / Accepted: 23 August 2022 / Published online: 6 September 2022

Abstract

In this work, we determined the coseismic slip distribution of the Boumerdes-Zemmouri earthquake (Mw 6.8, 2003) by inverting a most comprehensive set of data, teleseismic seismograms, strong motion seismograms, coastaluplift, Global Positioning System (GPS), and Interferometric Synthetic Aperture Radar. We suggest a best-fitting model of coseismic slip distribution on the following two segments: the first segment oriented at N70° and the second segment located at the west of the first one and oriented at N100°.The slip distribution shows two slip patches on the N70° segment containing the hypocenter. The eastern patch is shallower, located between 0 and 9 km depth, with a maximum slip of 2.30 m. The western slip-patch on this same segment is deeper, between 4 and 12 km depth, with a slip that reaches a maximum value of 2.70 m at the center. The N100° segment also displays two slip patches, a small one in the east of the segment, which is between 4 and 8 km depth and a larger one in the western part of the segment, between 0 and 10 km depth. Both patches associated with the N100° segment show a maximum slip between 1.10 and 1.40 m.

Keywords Waveform modeling · Rupture process · Boumerdes-Zemmouri · Coastal uplift · Geodetic data · Seismological data

1 Introduction

The Boumerdes-Zemmouri earthquake with Mw 6.8 occurred on 21st May, 2003 at 19:44 (UTC) and was relocated on the coastline at 36.83°N and 3.65°E (Bounif et al. 2004) at ~ 50 km east of Algiers (Algeria).

This earthquake is considered as the second strong earthquake that struck northern Algeria, after the El Asnam earthquake (Ms = 7.3) on 10 October 1980. The Boumerdes-Zemmouri event was the subject of many studies, among which several focused on seismic source analysis (Yelles-Chaouche et al. 2004; Meghraoui et al. 2004; Delouis et al. 2004; Semmane et al. 2005; Belabbes et al. 2009), or on the evaluation of the aftershocks' distribution (Bounif et al. 2004; Ayadi et al. 2008; Ouyed et al. 2011; Kherroubi et al. 2017). We note the 2003 rupture developed below the coastal area, partly under the sea. The Model suggested by Deverchère et al. (2005) described active structures observed on the Boumerdes offshore probablyactivated during the 2003 earthquake.

Different kinds of observations and measurements have been inverted jointly regarding the analysis of the rupture process of the 2003 earthquake. Different combinations of purely static displacement data such as GPS, InSAR (Synthetic Aperture Radar Interferograms) and coastal uplift were used to constraint the slip (Yelles-Chaouche et al. 2004; Meghraoui et al. 2004; Belabbes et al. 2009). Two other studies are available, which combined seismological and static displacement data (Delouis et al. 2004; Semmane et al. 2005).However, all the available data were never inverted altogether, in particular, strong-motion, teleseismic, and InSAR data.

This work is dedicated to the memory of our late Assia Harbi.

✉ Hamoud Beldjoudi
hamoud.beldjoudi@craag.edu.dz

Bertrand Delouis
delouis@geoazur.unice.fr

[1] Centre de Recherche en Astronomie Astrophysique et Géophysique (CRAAG), BP 63 Route de l'Observatoire Bouzaréah, Alger, Algérie

[2] Geoazur, Université de Nice, 250 Rue Albert Einstein, 06560 Valbonne, France

The motivation of this work is mainly twofold: (i) combine for the first time a most comprehensive set of data, including teleseismic, strong motion, GPS, InSAR, and coastal uplift, in order to better constrain the rupturing process; (ii) explore for the first time the possible offshore coseismic faults activation as described in Deverchere et al. (2005). Mahsas et al. (2008) proposed that post-seismic slip inferred from GPS measurements occurred between 0 and 5 km depth near the top of the coseismic rupture. Mahsas et al. (2008) suggest that the post-seismic deformation may have involved a shallow after slip, in agreement with the observed folding of the soft sediments following the 2003 earthquake (Deverchere et al. 2005). In this study, we explore the complexity of the 2003 Boumerdes-Zemmouri earthquake rupturing process, taking into account both previously published coseismic models and structural complexities of the earthquake rupture. In order to define an optimal model, we will assess the degree of the complexity of the rupture (model) that can be justified by the data.

In this work, we invert jointly, for the first time, a set of seismological (teleseismic and Strong-Motion) and geodetic data (GPS, InSAR and coastal uplift) to well constrain the coseismic slip of the Boumerdes-Zemouri earthquake. This study will permit us to confirm or not the last coseismic slip models obtained by various authors or to give us another model with a more complex slip.

2 Data

2.1 Teleseismic (TELE)

Eighteen broadband seismogram records of the mainshock at a teleseismic distance, ranging between 30° and 90°, are obtained from the IRIS and ORFEUS datacenters (Fig. 1a). The broadband stations are well distributed azimuthally. Seismograms were deconvolved from the instrument response, integrated into displacement and equalized to a common magnification and epicentral distance. Signals were bandpassed from 0.01 Hz to 0.8 Hz (P waves) or 0.4 Hz (SH waves). Finally, waveforms are windowed around P and SH wave trains separately.

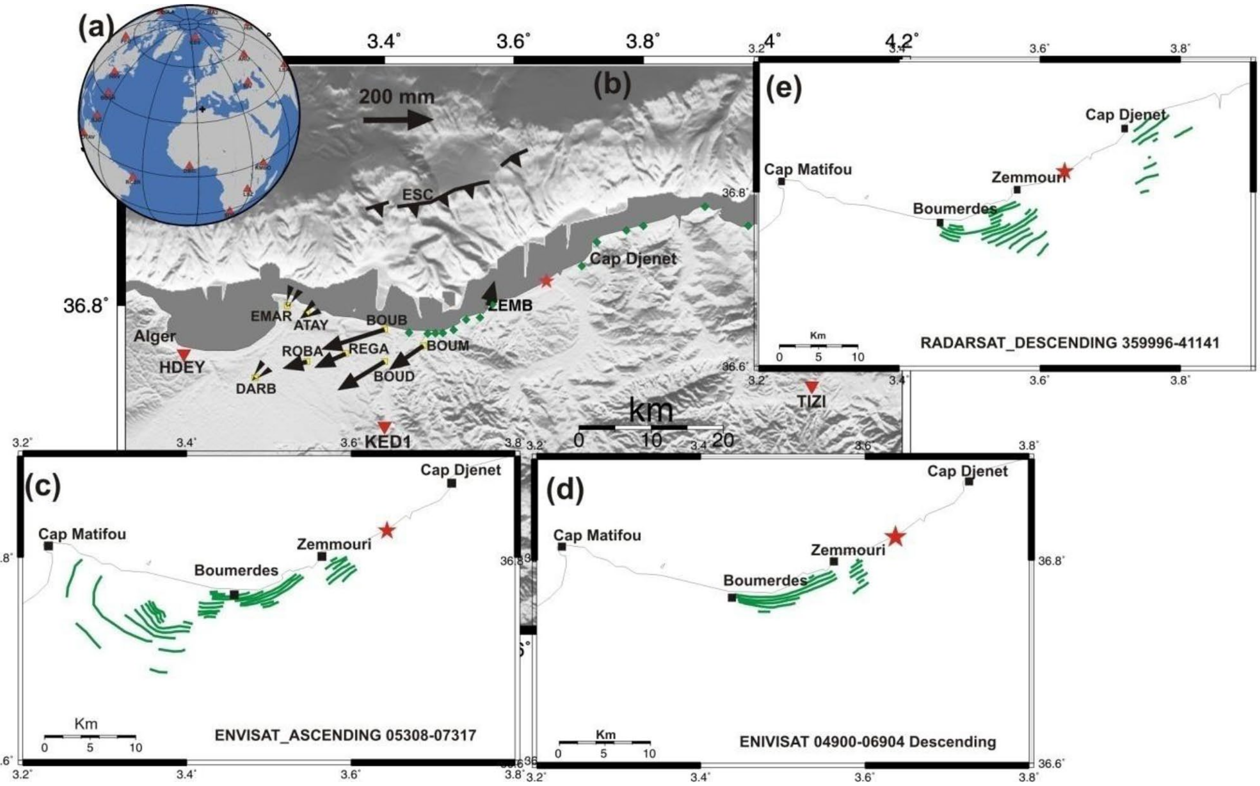

Fig. 1 Map showing the location of the datasets used in the joint inversion. **a** Red triangles are teleseismic stations. Black cross is the epicenter location. **b** Yellow squares are the GPS stations; location. Black arrows are the horizontal coseismic displacement vectors recorded at these stations. Green diamonds show the coastal uplift (CU) measuring points. Red inverted triangles are the strong-motion stations. Red star is the epicenter location of Boumerdes-Zemmouri earthquake on 21 May 2003. ESC: offshore escarpments B1 and B2 from Deverchère et al. (2005). **c–e** Green lines are digitized fringes from InSAR image: ENVISAT-Ascending, ENVISAT-Descending and RADARSAT-Descending, respectively

2.2 Strong motion (SM)

We use three strong-motion accelerograms from the Algerian earthquake engineering research Centre (CGS: Centre de Génie Parasismique) (Fig. 1b). Two of them (TIZI and HDEY) are analogic (SMA-1 instruments), and KED1 is a digital one (Altus, Etna).These stations work on triggered mode (not switch to a GPS clock time). Unfortunately, the first P wave was lost at all three stations (KED1, HDEY and TIZI, Fig. 1a, b). To overcome this limitation, we estimated the arrival time of the first P wave at each ostation by conducting a series of strong motion inversions. Since this estimation cannot be very accurate, we included in the inversion procedure the possibility of a time shift by up to 2 s of the seismic traces by performing a correlation between the observed and computed signals. Accelerograms are integrated twice to obtain displacement and related frequency components by applying a bandpass filter from 0.1 Hz to 0.25 Hz. The EW component of the TIZI station is affected by another problem, a discontinuity in the signal (Fig. 2), which could not be corrected. This component was hence excluded from the inversion procedure by assigning it a zero weight.

2.3 GPS

The coseismic horizontal displacements were obtained from Yelles et al. (2004), who processed 9 GPS sites (Fig. 1b). These sites are located between Algiers and Zemmouri, covering only a small portion of the rupture zone. The maximum horizontal coseismic slip displacement of ~ 20 cm, was observed at Boudouaou El Bahri site (BOUB). The vectors of displacement in all sites are oriented WSW except the site of Zemmouri El Bahri (ZEMB) which is oriented NNE.

2.4 Coastal uplift (CU)

Coastal uplift data are from Meghraoui et al. (2004). A shoreline uplift marked by a continuous white band visible at rocky headlands occurred during the 21 May 2003 earthquake (Mw 6.8). It was observed between Boumerdes and Dellys (Meghraoui et al. 2004). The coastal uplit is caused by a coastal reverse fault-oriented NE and plunging to the SE (Fig. 1b).The coastal uplift data show a maximum uplift of 0.75 m east of Boumerdes city and a minimum close to 0 m near Cap-Djenet.

2.5 Synthetic Aperture Radar Interferograms (SAR)

The SAR interferograms were processed by Belabbes et al. (2009) and consisted of digitized fringes from two descending and one ascending interferograms and incorporated into the inversion. Since fringes are discontinuous, we defined seven groups inside which fringes could be counted sequentially. We attributed a line-of-sight (LOS) displacement value to each fringe, making some assumptions about the position of the zero fringe. However, we allowed a LOS shift as a free parameter in the inversion for each of the seven groups. These LOS shifts allow correcting for possible inaccuracy in the assumption of the zero fringe, which may be difficult to identify in certain areas. The interferograms correspond to the following tracks (Belabbes et al. 2009): Envisat descending numbers 04900–06904, between 2003/02/06 and 2003/06/26; Envisat ascending numbers 05308–07312, between 2003/03/06 and 2003/07/24; Radarsat descending number 355996–40798, between 2002/09/27 and 2003/08/29. These three interferograms cover the epicentral area from Cap Matifou in the west to Cap Djenet in the east, but with large gaps in between (Fig. 1c-–e).

The InSAR Tracks that we use include about one month of the post-seismic period. Using GPS and GPS plus InSAR data, respectively. Mahsas et al. (2008) and Cetin et al. (2012) showed that post-seismic deformation can be explained by after slip occurring essentially offshore, between Boumerdes and Dellys, i.e. updip of the main coseismic slip areas. Our slip models show very little slip offshore in the area of afterslip, from which we conclude that the post-seismic deformation only marginally biases our coseismic models.

2.6 Common characteristics of fault models and inversion procedure

The rupture of the Boumerdes-Zemmouri earthquake was modeled using the kinematic fault approach of Delouis et al. (2002). The fault kinematic approach adopted in this study allows for multiple segments of rupture, each defined by its dimension, strike and dip angles, discretized by a regular mesh of point sources able to model the seismological data, and a mesh of rectangular subfault dislocations able to model the geodetic data. Each point source is defined by a local source time function (local STF)

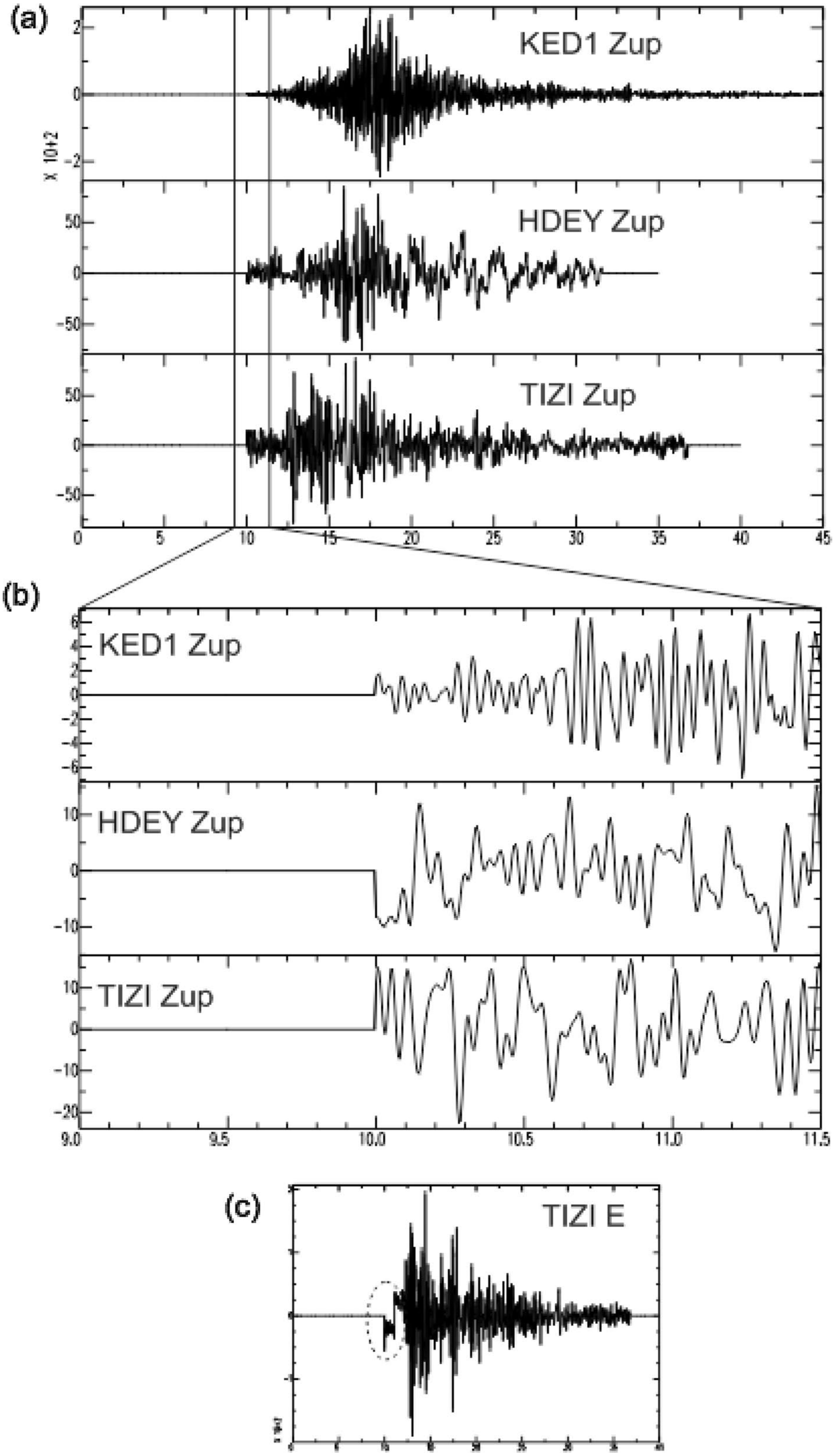

Fig. 2 particularity of the strong motion seismograms of the Boumerdes mainshock. **a** Complete acceleration time series for the vertical component of KED1, HDEY and TIZI stations. The three traces are aligned to start at $t = 10$ s for the purpose of illustration. **b** Zoom on the initial part of the same seismograms. Original seismograms had no absolute time reference and started where time is equal to 10 s on the graph. We completed the seismogram before original start (between 9 and 10 s on the graph) with zeroes. As can be seen, original seismograms started abruptly meaning that the initial P wave was lost. **c** Complete acceleration time series for the east component of TIZI station. We see that within a few seconds after start at $t = 10$ s, the seismogram displays two successive amplitude shifts (within the dashed ellipse), which bias the seismogram. This component will be discarded from the inversion

representing the seismic moment rate, the direction of slip (rake angle), and the rupture onset time. Each local STF is represented by three isosceles triangular functions of time-width 3 s, mutually overlapping. One of the point sources coincides with the earthquake hypocenter. For each point source (i.e. Subfault), we inverted the following: The rupture inset time, the Rake angle and the amplitudes of the three triangular functions. The allowed shifts of the seven fringe groups of the InSAR data are included in the inversion procedure. The simplest models will incorporate a single rupture plane (or fault segment), while the more complex ones will consist of several rupture planes (fault segments) with possibly variable dimensions, strikes and dips. Exploration of the parameter space is carried out with a simulated annealing algorithm (Corona et al. 1987). It requires the a priori definition of the range of values for the inverted parameters.

The convergence of the simulated annealing procedure is based on the minimization of a cost function (F_{cost}), corresponding to the weighted sum of the normalized RMS (root mean square) misfit function of each dataset, plus two functions, one minimizing the total seismic moment (F_{Mo}), the other smoothing the slip distribution (F_{smooth}):

$$F\text{cost} = \sum_{1}^{n_{\text{datasets}}} w_j \text{RMS}_j + bF_{M_0} + cF_{\text{smooth}},$$

where « n_{datasets}» is the number of datasets, j corresponds to the j^{est} dataset,«w_j» is the weight of the j^{est} dataset, b and c are two coefficients allowing to increase or decrease of the effect of the two associated functions.

The normalized RMS misfit function of each data set is defined as follows:

$$\text{RMS}_j = \sqrt{\frac{\sum_1^n \left(o_i - c_i\right)^2}{\sum_1^n \left(o_i^2\right)}},$$

where «n» is the number of data points in dataset «j»,, «O_i» and «C_i» the observed and computed values of data point «i», respectively.

The function minimizing the seismic moment is as follows:

$$F_{M_0} = e^{[\left(\frac{M0_{\text{mod}}}{M0_{ref}}\right)-1]},$$

with «$M_{0_{\text{mod}}}$» the total seismic moment of the model, «$M_{0_{\text{ref}}}$» a seismic moment of reference.

Table 1 Velocity models used in the modeling of strong motion records

Layer thickness (Km)	Vp (km/s)	Vs (km/s)	Density (g/cm^3)	Qp	Qs
Velocity Model for KED1 station					
0.5	4.5	2.6	2.5	150.00	75.00
10.00	5.00	2.89	2.60	300.00	150.00
23.50	6.50	3.71	2.70	400.00	200.00
0.00	8.00	4.62	2.78	1000.00	500.00
Velocity Models for HDEY and TIZI stations					
0.50	3.50	1.38	1.90	150.00	75.00
3.00	4.50	2.57	2.30	300.00	150.00
9.00	5.00	2.86	2.40	400.00	200.00
8.00	5.50	3.14	2.55	500.00	250.00
10.00	7.00	4.00	3.10	700.00	350.00
0.00	8.00	4.57	3.40	1000.00	500.00

The smoothing function (F_{smooth}) is simply the normalized sum of the differences in slip values between each subfault and its adjacent subfaults.

Since each dataset is normalized in the RMS function, we use the same weight (w_i) for each dataset.

The smoothing coefficient (c) is adjusted by performing synthetic data inversions and retaining the coefficient providing the best fit between the inverted and synthetic input models.

Synthetic (computed) seismograms at local to regional distances (strong motion data) are generated with the discrete wavenumber method of Bouchon (1981) designed for 1D velocity models. Velocity models were initially derived from published models (Bounif et al. 2004; Semmane et al. 2005), but we modified them to obtain an optimized model per station, in particular, adding a low-velocity shallow layer below HDEY and TIZI (Table 1).

For the teleseismic record, synthetic seismograms are computed using the ray theory with the method of Nabelek (1984) using homogeneous half space models for both source and stations.

To compute synthetic static ground displacement, used to model the geodetic data, we follow the formulation of dislocations embedded in the elastic half-space of Savage (1980).

2.7 Faults modeling and results

The main geometric parameters (strike, dip, length, and width) of the various models tested in this study are given

Table 2 Geometry and dimension of the fault model

	Strike (deg.)	Dip (deg.)	Length (km)	Width (km)	Length and Width of subfaults (km)
Model one segment					
Segment 1	70	40	60	24	4×4
Model two segments					
Segment 1 (N70° segment)	70	40	60	24	4×4
Segment 2 (N100° segment)	100	45	56	24	4×4
Model 4 segments					
Segment 1 (N70° segment)	70	40	60	24	4×4
Segment2 (N100° segment)	100	45	48	24	4×4
Segment 3 (flat segment)	70	8	60	12	4×4
Segment 4 (ramp segment)	70	50	60	04	4×4

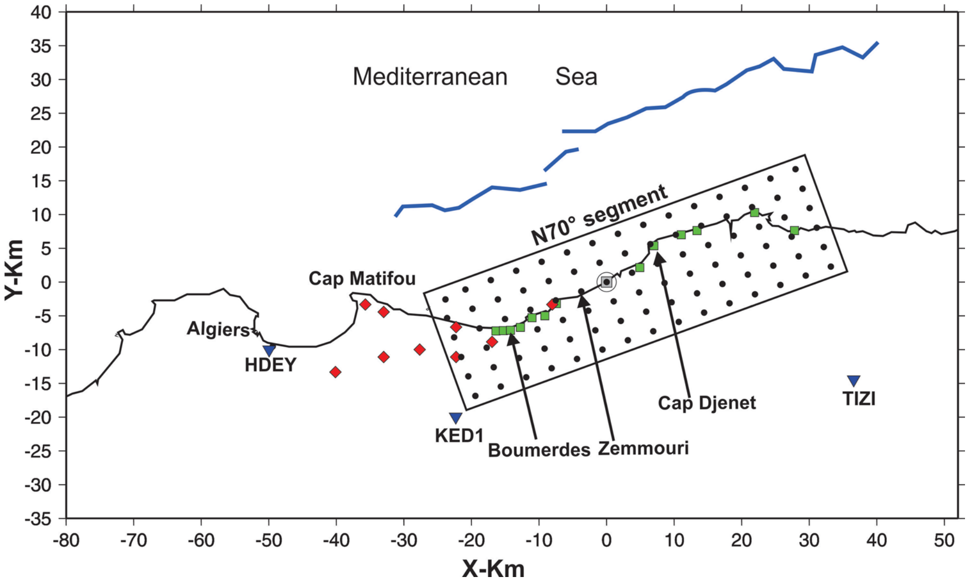

Fig. 3 Surface projection of model 1seg (rectangle), with black dots corresponding to the point sources at the center of the subfaults. Grey square within an open circle: subfault corresponding to the hypocenter; black line: coastline; blue lines: offshore escarpments B1 and B2 described in Deverchère et al. (2005); red diamonds: GPS stations; green squares: points where coastal uplift was measured (Meghraoui et al. 2004); black inverted triangles with names: strong motion stations. *Y axis* is oriented towards the north

in Table 2. The RMS misfit functions relative to the different datasets used in the joint inversion are presented in Table 3. In all fault models, we consider the position of hypocenter as fixed. The epicenter had been relocated on the coastline at 36.83°N and 3.65°E by Bounif et al. (2004). The hypocentral depth constrained by the teleseismic data is the same as in Delouis et al. (2004). In all cases, the rake is allowed to vary between + 80° and + 110°, except for the N100° segment (see below), where the rake is between + 75° and + 105°. We will not show the slip vectors on the slip maps since they do not vary much. Rupture timing can vary according to a minimum and maximum rupture velocity, respectively, $V_{\mathrm{rmin}} = 1.6$ km/s and $V_{\mathrm{rmax}} = 3.5$ km/s. For a given subfault, the rupture velocity considered here is the distance to the hypocenter divided by the rupture onset time.

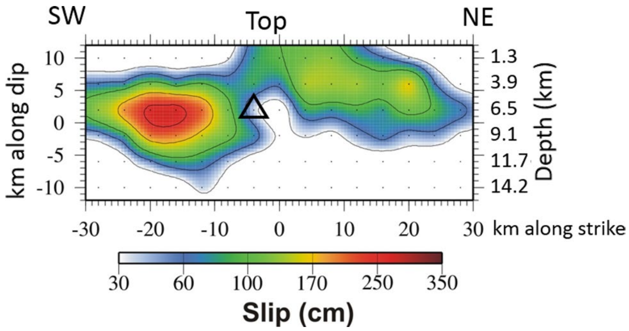

Fig. 4 Slip distribution from the joint inversion of all datasets with 1seg model. The open triangle indicates the point source corresponding to the hypocenter. Black dots correspond to the point sources at the center of the subfaults

2.8 One segment model (1seg)

As a starting model, we use the same model as published in Delouis et al. (2004), hereafter called "Delouis-2004". However, this model is tested with two additional datasets, strong motion and InSAR. The fault model dimensions are the same and consist of ~ 60-km-long and ~ 24-km-wide at the exact position of each dislocation as in Delouis et al. (2004) (Fig. 3). Nonetheless, the rupture model is discretized more finely than the original model, with subfaults measuring 4 km × 4 km instead of 6 × 6 km. This is because we included the near-fault SM and SAR data.

We carried out tests varying the strike of the fault around the value used in Delouis-2004 (70°) but with joint inversions of all the datasets (TELE, SM, GPS, SAR, CU). Strikes between 65° and 75° produced equivalent quality results. Consequently, we retain 70° as the optimum strike, as in Delouis-2004. On the other hand, fault dip was fine-tuned to 40° (instead of 45° in Delouis-2004). This compromise is due to the fact that the value of 45° slightly improves the modeling of the GPS data but degrades the modeling of the seismological data. Note that the top of the fault model reaches the surface offshore.

Based on the positioning of the fault model along the coast, models located farther offshore like the one used in Semmane et al. (2005) produce a clear degradation of the modeling of the teleseismic data. The reason is that a more offshore models require a deeper hypocenter (> 10 km), and this will affect directly the fitting between the synthetic and observed teleseismic seismograms.

The slip distribution is shown in Fig. 4. It is similar to that of Delouis-2004, with a main slip patch west of the hypocenter, with slip reaching 2.80 m, and a shallower patch east of the hypocenter. However, we note that the slip extends slightly farther west. Regarding data modeling, we encountered difficulty in achieving a good fit of the complete set of

Fig. 5 Modeling of the GPS horizontal vectors obtained from the joint inversion of all datasets with 1seg model. The results from Delouis et al. (2004) are in the upper left corner for comparison. Same color scale for slip as in Fig. 4

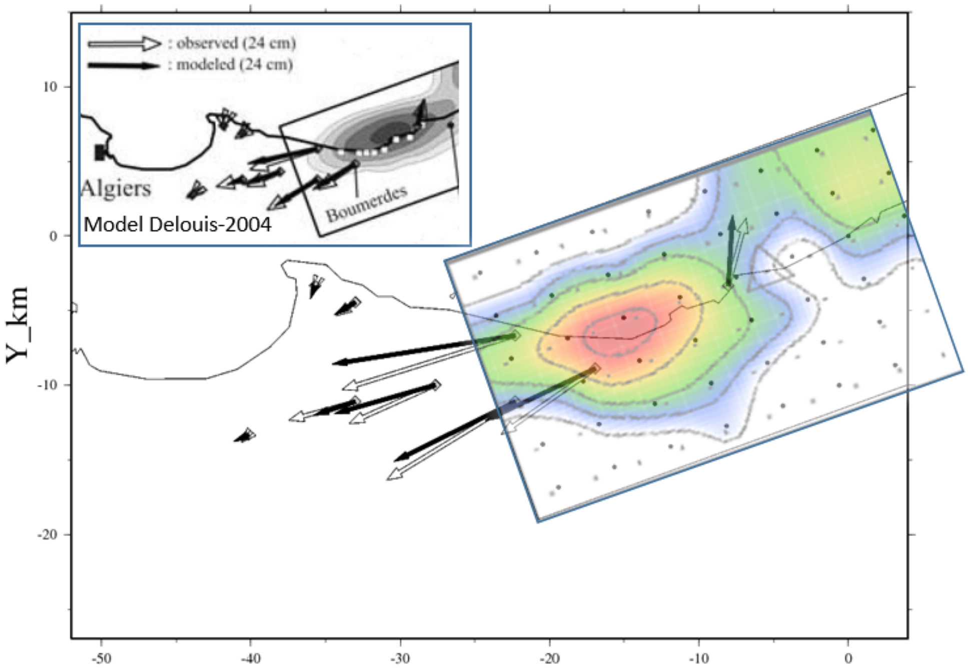

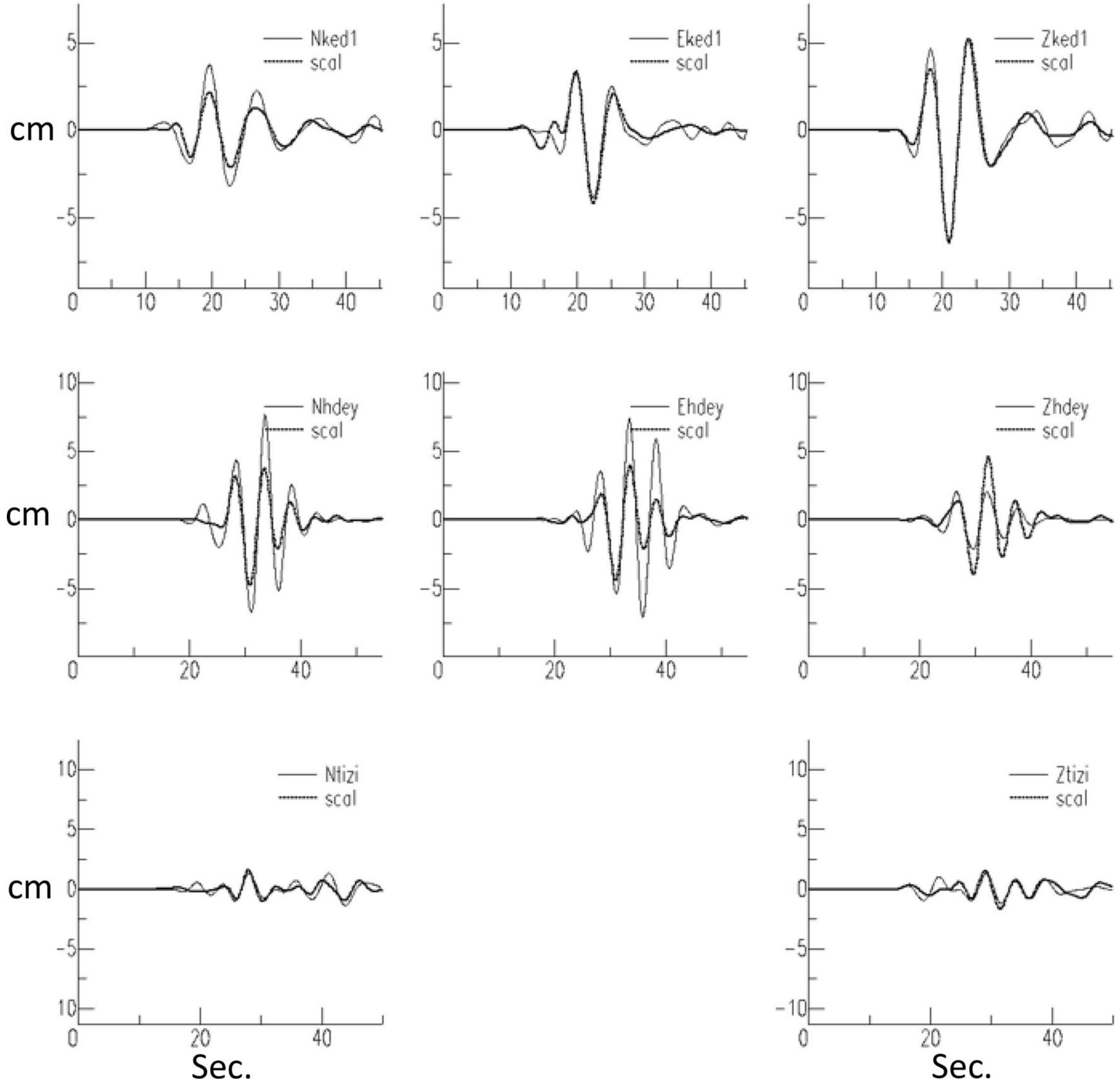

Fig. 6 Modeling of displacement waveforms from the strong motion records obtained with the joint inversion of all datasets with respect to the model 1seg. The east component of station TIZI is not shown since it was discarded due to seismogram artifacts (Fig. 1c). Amplitudes are in cm, time in seconds. Gray line represents the observed seismogram; the heavy black line represents the computed seismogram

data. We will not show the modeling of all the datasets with this initial model but will focus on specific problems. The fit of GPS data is slightly degraded with respect to that in Delouis et al. (2004) (Fig. 5). This is due to the dip value of 40° instead of 45° and to the fact that we include the additional SM and SAR datasets. The overall average rupture velocity, weighted by the slip values, is 2.5 km/s.

Additionally, we observe difficulty incorrectly modeling SM station HDEY (Fig. 6). The modelled signal bypasses the first pulses on the horizontal components, and the overall amplitudes are not matched at that station. The same difficulty in modeling HDEY was found in Semmane et al. (2005).

Fig. 7 Surface projection of model 2seg. For other elements, same caption as Fig. 3

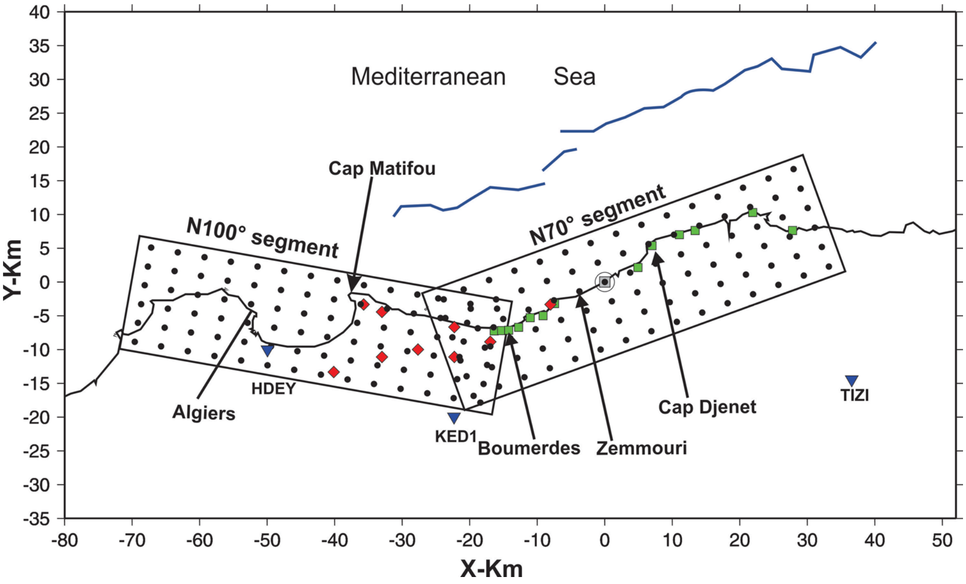

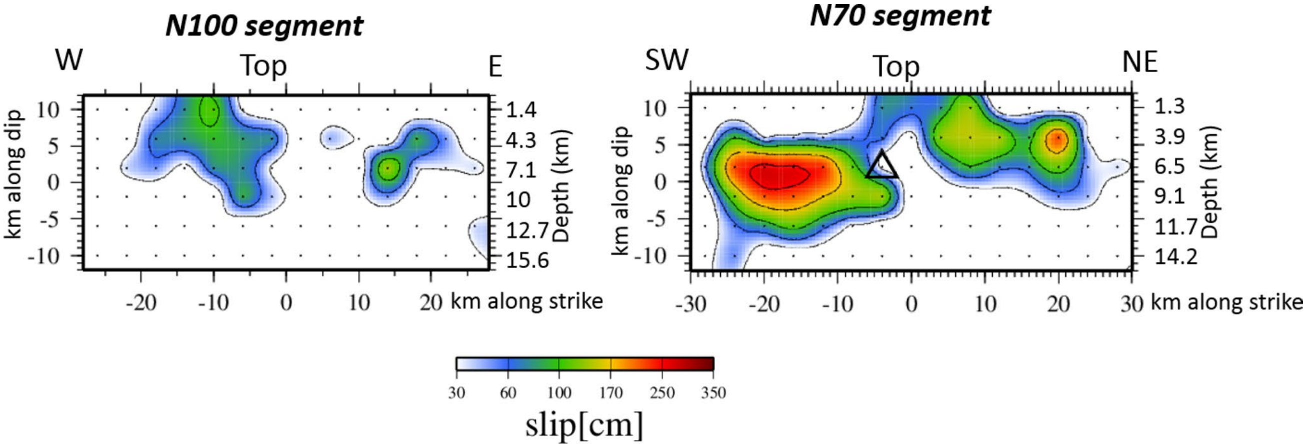

Fig. 8 Slip distribution from the joint inversion of all datasets with 2seg model.For other elements, same caption as Fig. 4

Fig. 9 Surface projection of the slip distribution obtained by joint inversion of all datasets with model 2seg. For other elements, see captions of Fig. 3. Same color scale for slip as in Fig. 8, but drawn with transparency

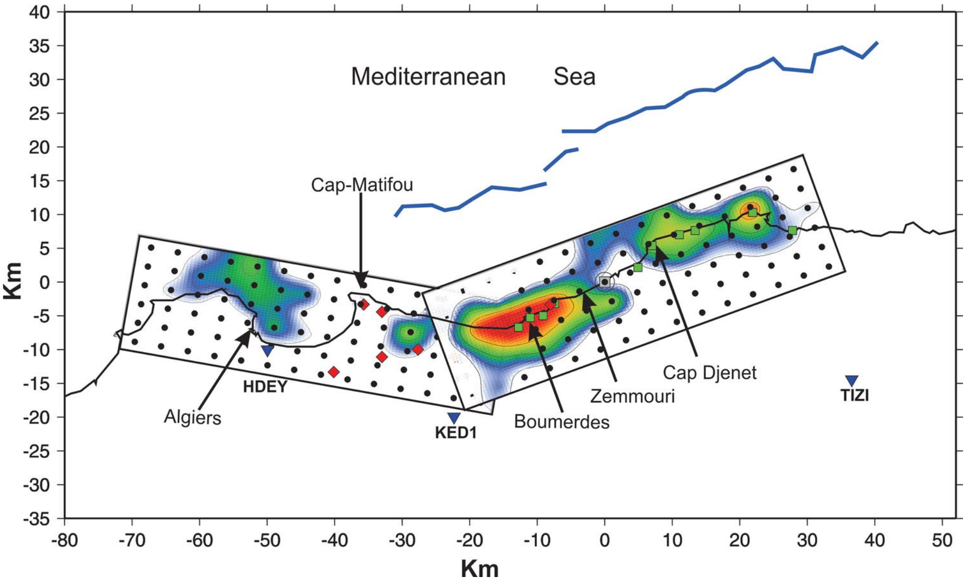

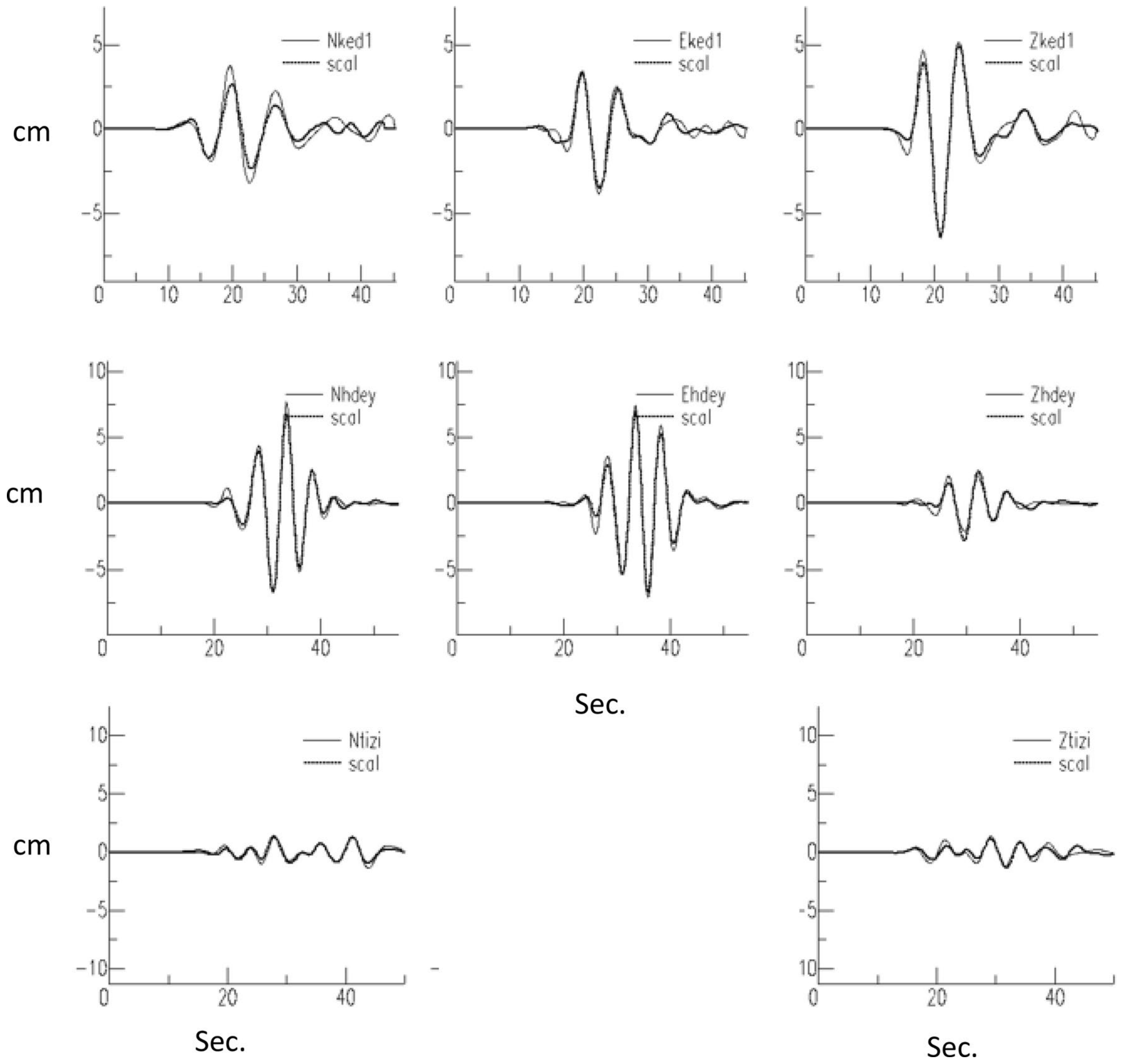

Fig. 10 Modeling of displacement waveforms from the strong motion (SM) records obtained with the joint inversion of all datasets with model 2seg. The east component of station TIZI was is not shown since it was discarded due to artifacts in the seismogram (Fig. 1c). Amplitudes in cm, time in seconds

The SAR data are well modelled, with a very low normalized RMS misfit function (Table 3). It seems that the SAR data do not require more complexity in the fault model, but the problems in the modeling of the GPS and SM (mainly HDEY) data suggest that the simple 1seg model cannot satisfy all the datasets together.

We also tested models with a longer fault, extending farther to the south-west, but it did not produce substantial improvements.

2.9 Two-segment model with a change in the strike (2seg)

In order to invert jointly purely geodetic data (SAR, GPS, and CU), Belabbes et al. (2009) proposed a rupture plane which curves in its western part. Their slip model trends NE–SW (~N60°) between Dellys and Boumerdes and changes to WNW–ESE (~N100°) between Boumerdes and

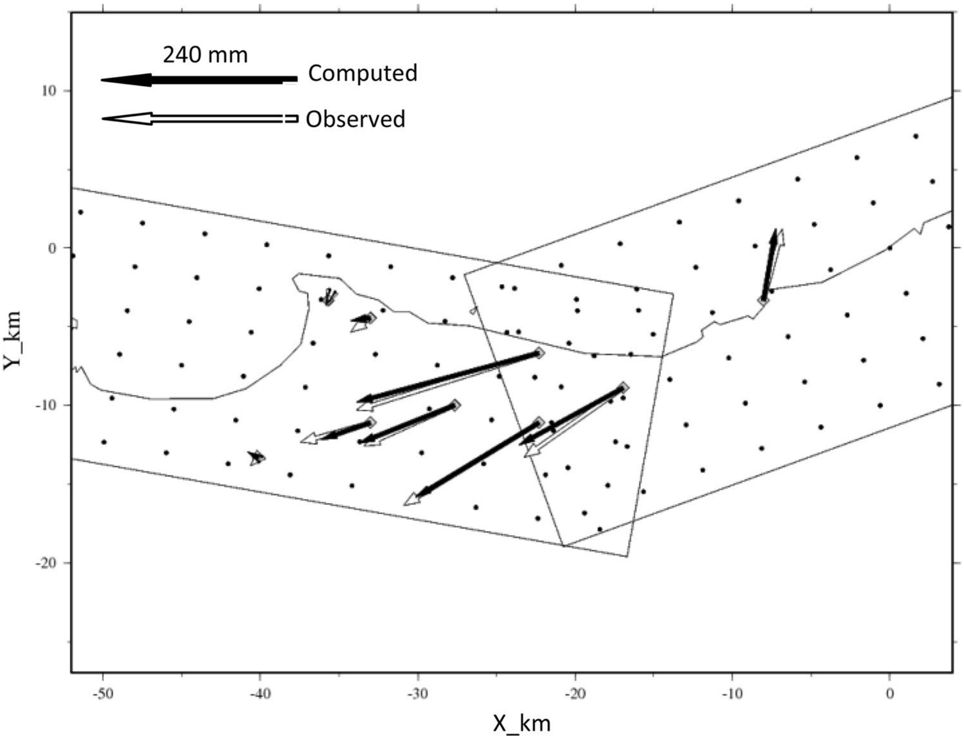

Fig. 11 Modeling of the GPS horizontal vectors from the joint inversion of all datasets with respect to the model 2seg

Cap Matifou. It is remarkable that the trend of the coastline changes in the same way near Boumerdes, so their model follows approximately the curve of the coastline.

In this section, we test such a change in the strike of the rupture plane, investigating, in particular, its effect on the modeling of the seismological data, which were not included in Belabbes et al. (2009). We decompose the model into two segments, a first one trending N070° (*N70° segmen*t), identical to our previous model 1seg, and a second one trending N100° (*N100° segment*). We tested different positions for the *N100° segment*, moving it in the inland direction or locating it more offshore, with a dip angle of 40°, 45°, or 50°. These tests were carried out with joint inversions of the whole dataset (TELE, SM, GPS, SAR, CU). The dip and position providing the best overall fit of the data are 45° and the location shown in Fig. 7, respectively. The two fault segments exhibit some overlap in the Boumerdes area, while the total slip map do not present overlap between the segments (Fig. 8).

The slip distribution (Fig. 8) shows two slip patches on the *N70° segment* containing the hypocenter. The eastern patch is shallower, located between 0 and 9 km depth, with a maximum slip of 2.30 m. The western patch on this same segment is deeper, between 4 and 12 km depth, and the slip reaches 2.70 m at its center. *The N100° segment* also displays two slip patches, a small one in the east of the segment located between 4 and 8 km depth and a larger one in the western part of the segment, located between 0 and 10 km depth (Fig. 9). Maximum slip lies between 1.10 and 1.40 m in both patches of the *N100° segment.*

The modeling of the SM data, in particular the HDEY station, is strongly improved (Fig. 10), while the clockwise rotation of the computed GPS largest vectors relative to the observed ones found with the 1seg model (Fig. 5) is strongly reduced (Fig. 11).

The modeling of the InSAR data set sampled from the fringes of three SAR interferograms (Fig. 12) shows the best fit between observed and computed fringes computed with the 2*seg*model (Figs. 13 and 14). The same remark can be done for the (CU) data set where the 2*seg* model suggested the best fit (Fig. 15).

The waveforms data set for the P and SH waves in displacement present the best fit between observed and computed synthetic obtained from the *2seg* model (Fig. 16).

Figure 17a shows the space and time évolution of the rupture, with cumulative snapshots every 3 s. This figure provides a vision of the propagation of “significative” slip, considered larger than 0.30 m. The actual rupture front,

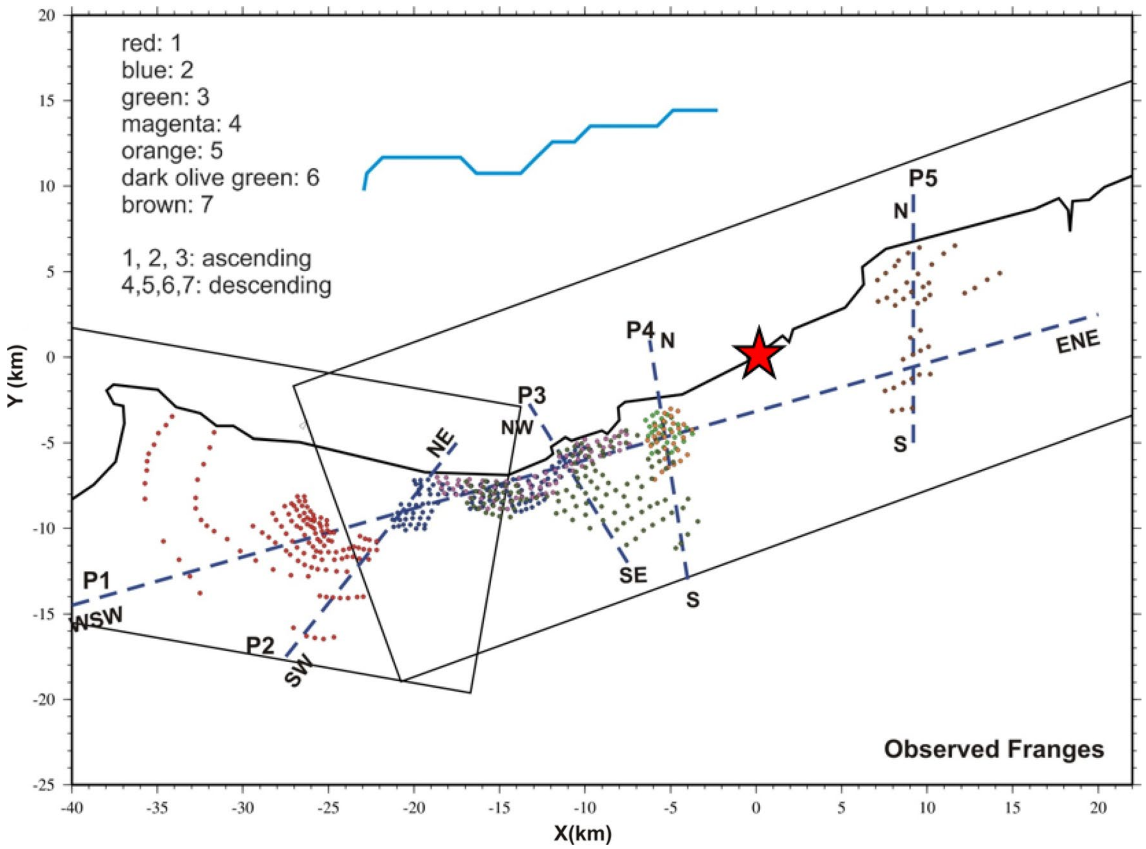

Fig. 12 InSAR data points sampled on the fringes of the three SAR interferograms included in the inversion. InSAR points are distributed among seven distinct groups plotted with different colors. Black dotted lines are five profiles used to show the InSAR data fit in Fig. 12. Red star: hypocenter of the mainshock; black line: coastline; blue lines represent the offshore escarpments B1 and B2 as described in Deverchère et al. (2005). Rectangular frames represent the part of the surface projection of the model 2seg boundary elements

related to the propagation of smaller slip values and connected to the rupture onset time of the subfaults, maybe slightly ahead of it.

As shown by the reference rupture front propagating at 2 km/s (red dashed line of Fig. 17a), we note that on the westernmost slip patch andfor a time $t = 18$ s, therupture velocity jump to 3.5 km/s.

The rupture on the N70 main segment is clearly bilateral, and it propagated faster toward the NE than toward the SW (see slip ahead of the 2 km/s front in the NE at $t = 9$ and 12 s).In this segment, slip evolves only marginally after $t = 15$ s.

Rupture on the N100 segment starts at about $t = 12$ s. On this segment, we observe a shallow slip patch initiating in the west well ahead of the 2 km/s front at $t = 18$ s. As indicated on Fig. 17a, the rupture velocity at this point is of the order of 3.5 km/s.

The global source time function (STF) shows the main pulse with a duration of 15 s, corresponding essentially to the rupture of the main N70 segment, and a continuation until 30 s, corresponding mainly to the rupture of the secondary N100 segment (Fig. 17b).

If we assumerupture velocity as the distance from the hypocenter divided by the rupture onset time of the subfaut, and if we average the rupture velocity of several subfaults weighted by their slip values, we find that the following:

– the overall average rupture velocity is 2.6 km/s,

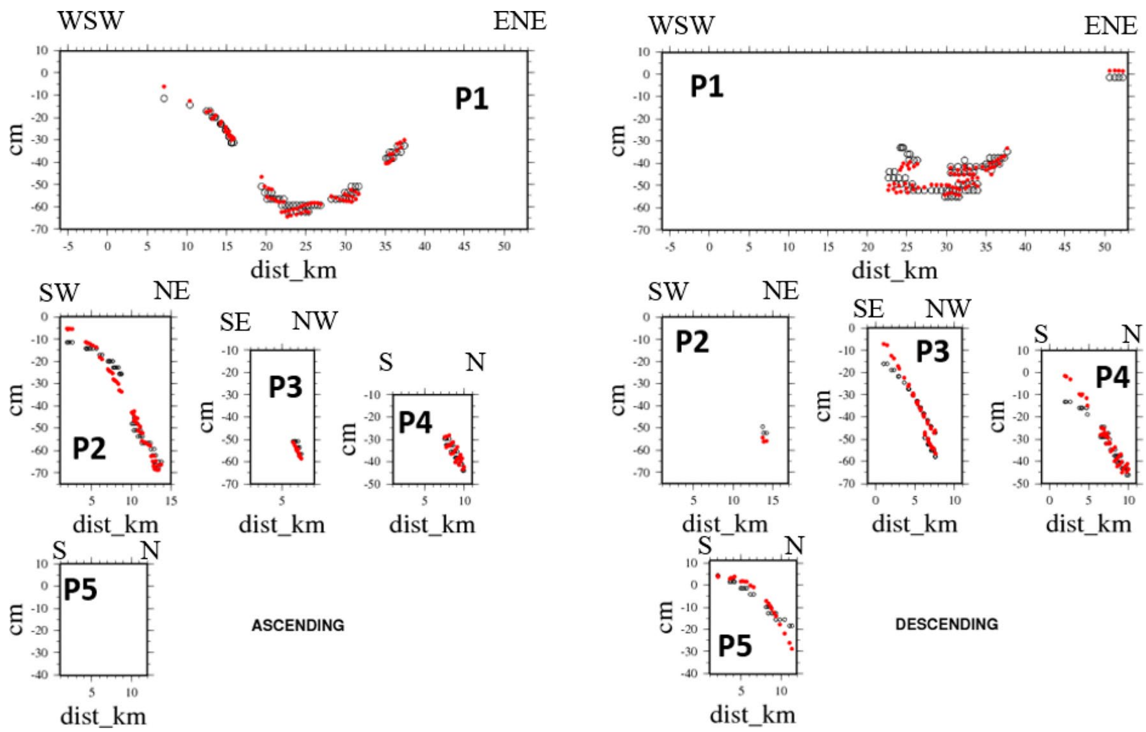

Fig. 13 Modeling of the InSAR data from the joint inversion of all datasets with model 2seg, seen along five profiles. Left: from the ascending interferogram; right: from the two descending interferograms. Open circles: observed data; red points: computed data. Vertical axis is the LOS (line of sight) displacement. Negative LOS values mean shortenning of the ground-to-satellite distance and are explained at the first order by coseismic uplift. Horizontal axis is distance along profile, with an arbitrary origin

- on the N70° segment, the average rupture velocity is also 2.6 km/s, but it is 2.8 km/s NE of the hypocenter and 2.5 km/s SW of it,
- on the N100° segment, the average rupture velocity is 2.5 km/s.

The average rupture velocity on the N100° segment is not meaningful given the differentiated behaviour of the two slip zones observed on this segment.The westernmost slip patch is initiated very early since the corresponding rupture front is associated with a rupture velocity of 3.5 km/s (see above).

If we carry out similar inversion technics but with a zero weight for station HDEY (i.e. station not taken into account), the slip area north of HDEY(i.e. north of Algiers in the western part of the N100° segment) disappears in the resulting model (Fig. 18). However, as shown in Fig. 19, the fit of HDEY records is then poor, the computed waveforms lacking amplitude in their last part. The same mismatch was observed in the modeling of Semmane et al. (2005) for the HDEY station (Fig. 20).

On the other hand, the GPS data remain well modelled (see RMS value in Table 3). We conclude that the westernmost slip patch on the N100 segment, located offshore Algiers, is required by station HDEY and only by that station. Note that the SM station HDEY is the only measuring point available in the west near Algiers.

We questioned whether the existence of this westernmost slip patch could be an artefact related to an inappropriate estimation of the *P* wave arrival on HDEY. We ran different inversion procedures with different variable time-windows for all strong-motion stations. We note that the slip patch was systematically found for these inversions.

We note that the RMS of the teleseismic data increases when SM station HDEY is not used in the inversion procedure (Table 3). This means that station HDEY, when used, helps find a solution even more compatible with the teleseismic data. This comforts us in the idea that station HDEY contains meaningful information and has to be retained.

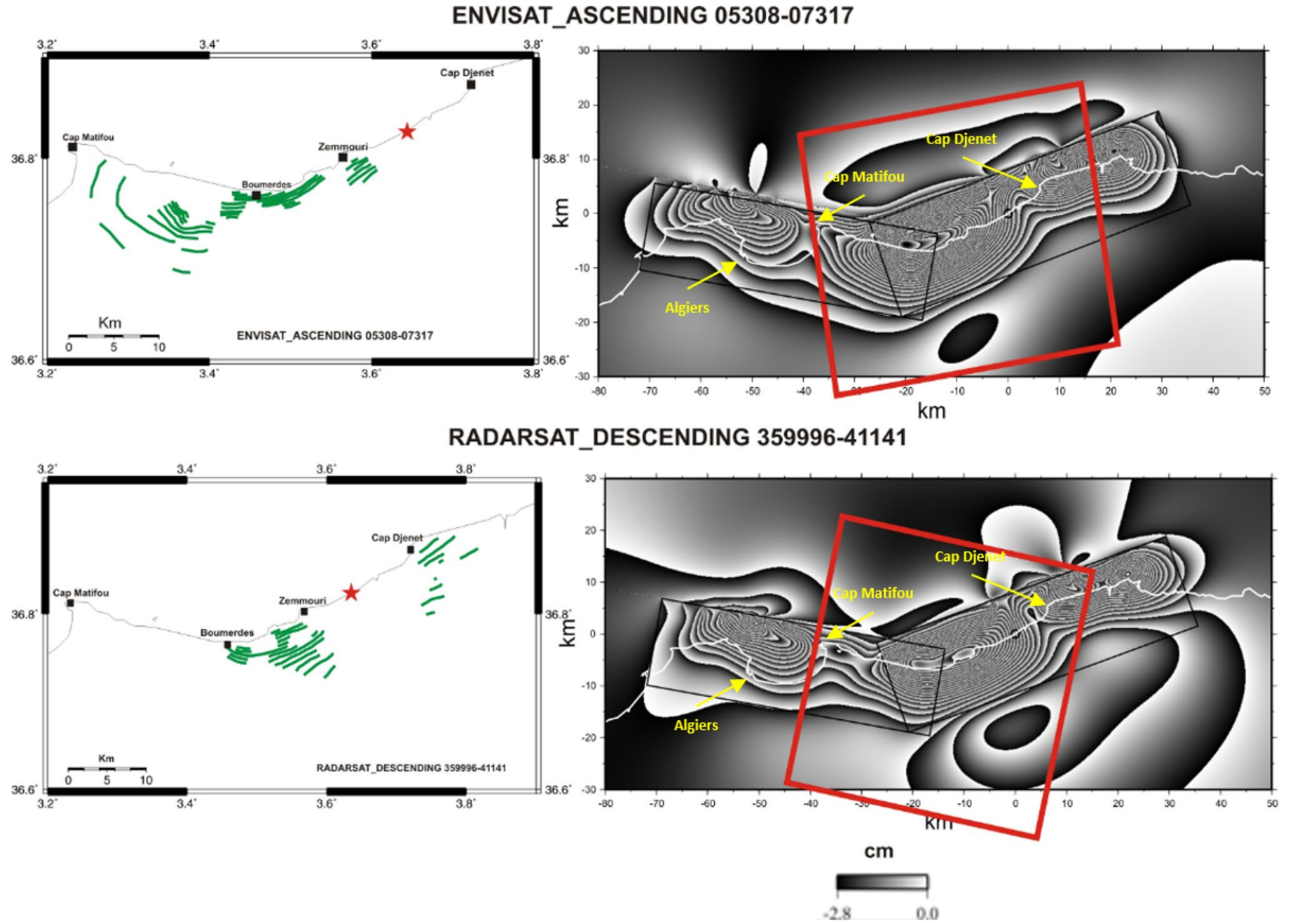

Fig. 14 Top left represents thedigitized Envisat ascending fringes (green lines). Red star: mainshock epicenter. Top right: computed Envisat ascending interferogram from the joint inversion with model 2seg of all datasets, each fringe corresponding to 2.8 cm of LOS displacement. The red frame is the positioning of the SAR track. Black rectangles show the surface projection of the 2seg model. White line: coastline. Bottom left and right: same at top, but for the Radarsat descending interferogram

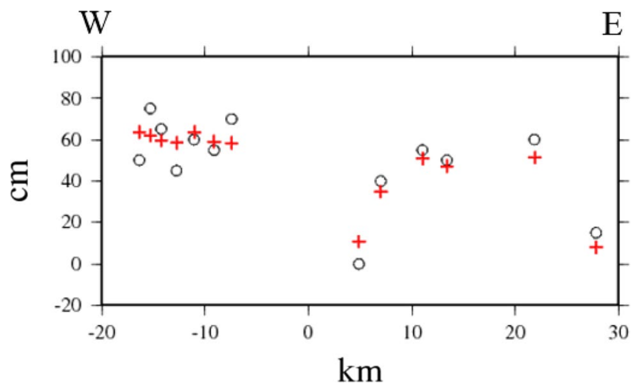

Fig. 15 Modeling of the coastal uplift (CU) measurements from the joint inversion with model 2seg of all datasets. Measuring points are located along the coast (Fig. 7). Horizontal axisrepresents the kilometers in the EW direction, with an arbitrary origin. Vertical axis represents costal uplift. Open circles represent observed data. Crosses are the computed data

2.10 Four segment model with flat and ramp offshore (4seg)

Through the combined analysis of high-resolution bathymetry and seismic reflection surveys, Deverchère et al. (2005) identified escarpments outcropping offshore the Boumerdes-Zemmouri area displaying evidence of recent seismic activity. According to these authors, the escarpments are likely related to a propagating fault system at shallow depth, revealing a ramp – flat geometry, associated with the folding and growth of the Plio-Quaternary sediments.

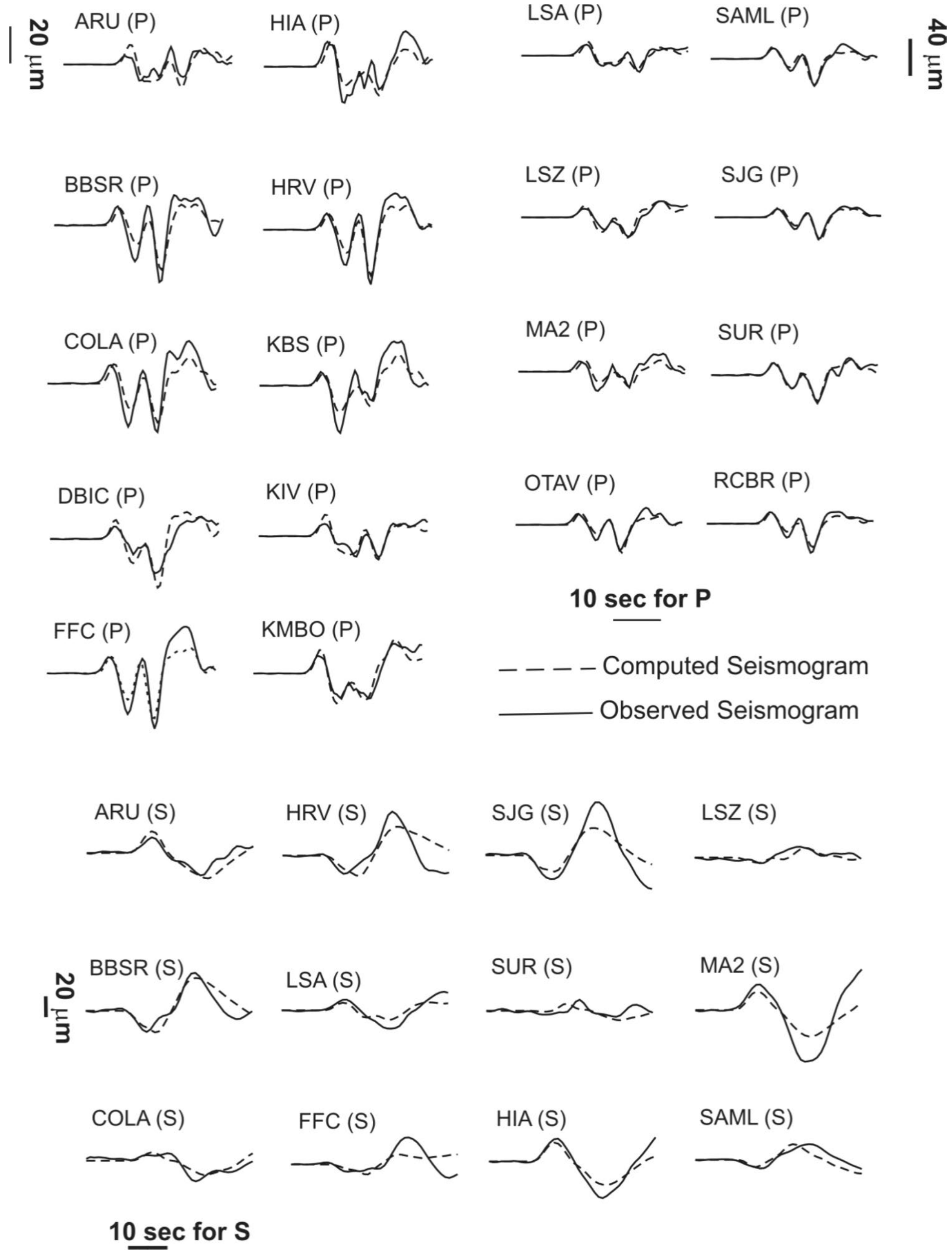

Fig. 16 Waveform fit for the P and SH waves in displacement, from the joint inversion with model 2seg

We constructed a model following the geometry of faults offshore proposed by Deverchère et al. (2005), with a shallow ramp reaching the surface where these authors locate their B1 and B2 escarpments (Fig. 21). The ramp segment, striking N70° and dipping 50°S, connects at about 3 km depth to a flat segment striking also N70°, dipping 8°S, which in turn connects to our main N70° segment at about 5 km depth (Fig. 22). The parameters of the complete model are presented in Tables 2 and 3.

The resulting slip model is presented in Fig. 23.

As shown in Fig. 23, the slip distribution on the N70° segment of the 4seg model is similar to what was obtained in the previous 1seg and 2seg models (Figs. 4 and 8). On the N100 segment, we observe two slip areas again, as in the

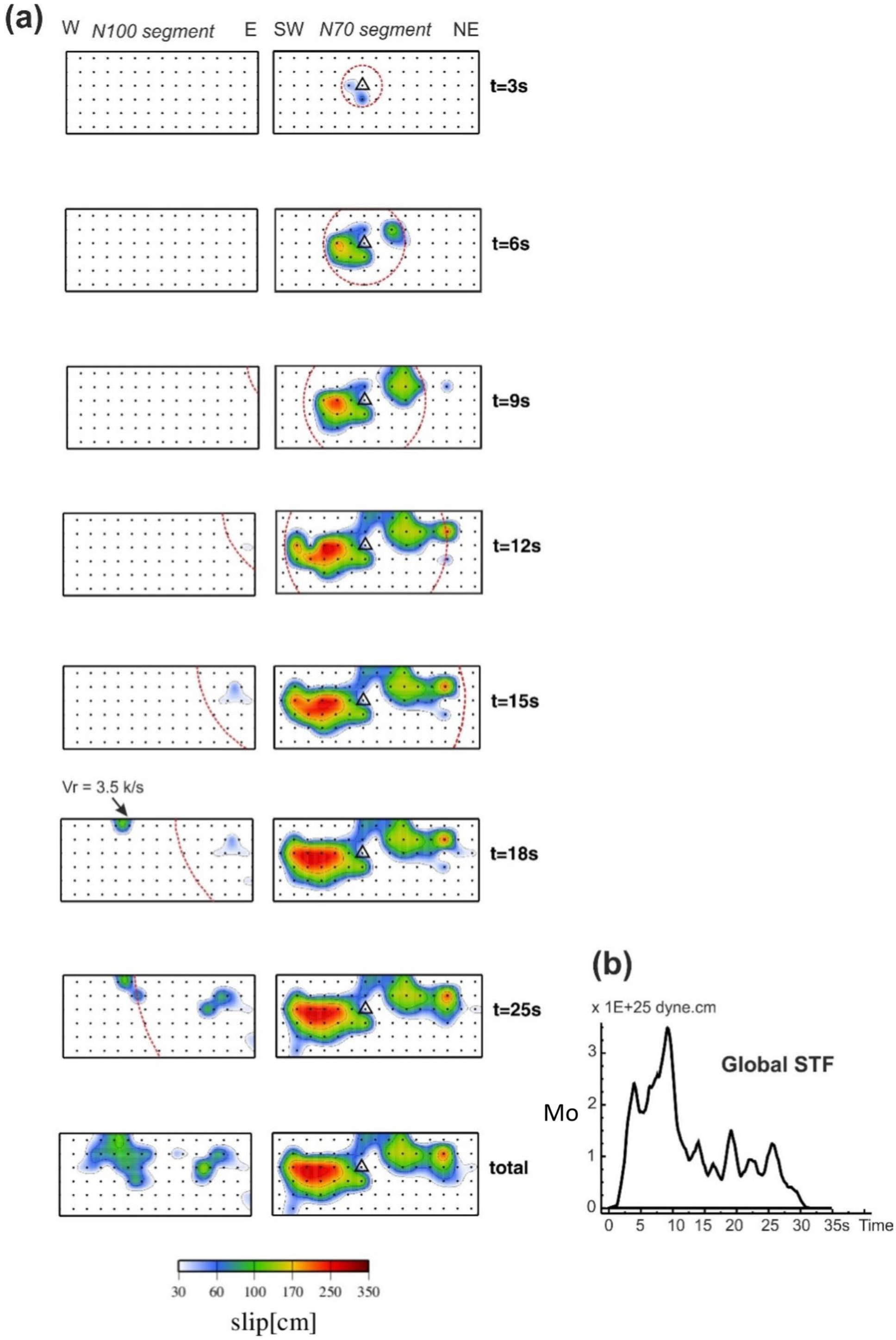

Fig. 17 **a** Space and time évolution of the rupture from the joint inversion of all datasets with model 2seg. Slip is displayed on the two segments with cumulative snapshots every 3 s. “Total” means the final slip distribution once rupture termination. The red dashed line shows a rupture front corresponding to a constant rupture velocity of 2 km/s, for reference. The initiation of the westernmost slip patch on the N100° segment is associated with a rupture velocity of 3.5 km/s as indicated at t = 18 s. **b** corresponding global source time function (STF)

2seg model (Fig. 23), although the shape of the westernmost asperity is different. This indicates that this westernmost slip patch, a persistent feature when SM station HDEY is considered, cannot be resolved in too much detail. This will be confirmed by the resolution tests. Slip on the two offshore segments is very limited, below 0.2 m on the *ramp segment* and reaching 0.5 to 0.6 m on localized small slip patches on the *flat segment* (Fig. 23).

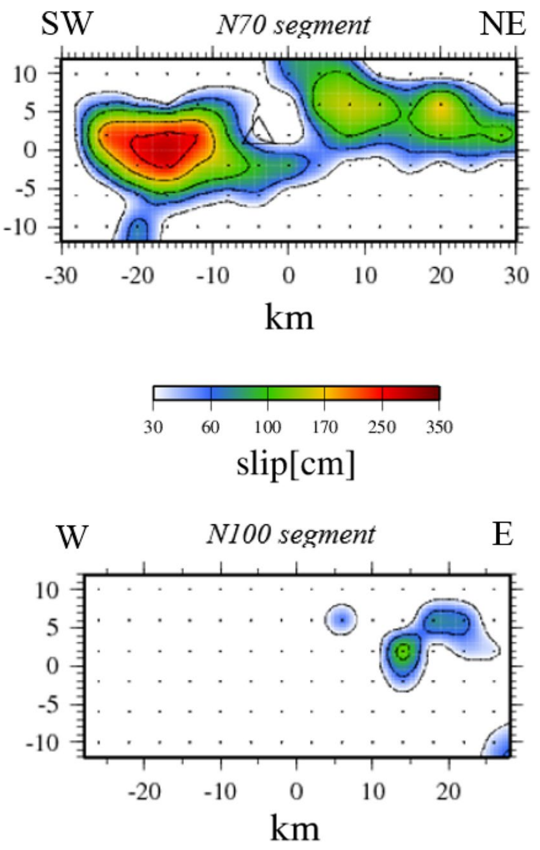

Fig. 18 Same as Fig. 8 but without station HDEY to which a zero weight is attributed

Data modeling is only marginally improved with respect to the 2seg model, as shown by the RMS misfit values in Table 3. Considering that the 4seg model is more complex than the 2seg model, with more parameters, without noticeable improvement in data modeling, and very few slips on the supplementary *ramp* and *flat segments,* it is not easy to confirm the validity of the 4seg model. Model 2seg, simpler and fitting the data equally well, may be considered a preferred model. We remind that the 2seg model obtained in this study is comparable with the curved model suggested by Belabbes et al. (2009).This is why we do not show the modeling of the different datasets with the 4seg model.

2.11 Resolution tests with synthetic data

In order to assess how the different datasets resolve the slip distribution and to which extent the joint inversion allows to resolve it better, we carried out a series of inversions of synthetic data. A synthetic slip model is constructed, with slip patches located on the different segments of the model. This synthetic model is used to generate synthetic data which are finally inverted with the same parameterization as for the real data inversions. Synthetic inversions were carried out with different smoothing coefficients, searching for the coefficient which minimized the root mean square difference between the synthetic and inverted slip distributions, both for the slip amplitude and rupture timing. All the results presented in this study, obtained with synthetic or real data, were carried out with this optimal coefficient of smoothing.

We applied this approach to the 2seg and 4seg models. The choice of these two models is motivated by the fact that the 2seg model can explain most completely all the real datasets, and to assess the slip on the offshore segments for the 4seg model.

2.12 2seg model

For the 2seg model, we performed six inversions of synthetic data, testing all five datasets (TELE, SM, SAR, GPS, CU) individually and jointly (Fig. 24). The synthetic slip model is characterized by five asperities numbered a1 to a5 (Fig. 24) with different shapes distributed on the two segments.

The inversion of the teleseismic synthetic data exhibits a “blurred” and spread-out version of the three slip patches on the N70° segment and a weak and mislocated slip zone on the N100° segment.

The inversion of strong motion synthetic data resolves better the three slip patches on the N70° segment, although with a lack of amplitude on asperities a1 and a3. On the N100° segment, the two slip patches asperity a4 and asperity a5 are found but weaker and deeper than in the synthetic model.

The inversion of synthetic coastal uplift data retrieves three asperities on the N70° segment, which tends to overestimate the maximum slip on asperities a1 and a3. Furthermore, the asperity a1 is replaced by a twin slip zone, with a deep part near the bottom of the mislocated model. Nothing is retrieved on the N100° segment. It is related to the absence of coastal uplift measuring points in the west above this segment (Fig. 7), and to the fact that the total seismic moment is minimized, avoiding effectively false slip where slip is not required by the data.

The inversion of GPS data does not find slip on the eastern part of the N70° segment (slip zones a2 and a3), also because GPS measuring points are absent in this area (Fig. 7). However, it resolves approximately slip zone a1 and the two slip zones (a4 and a5) on the N100° segment.

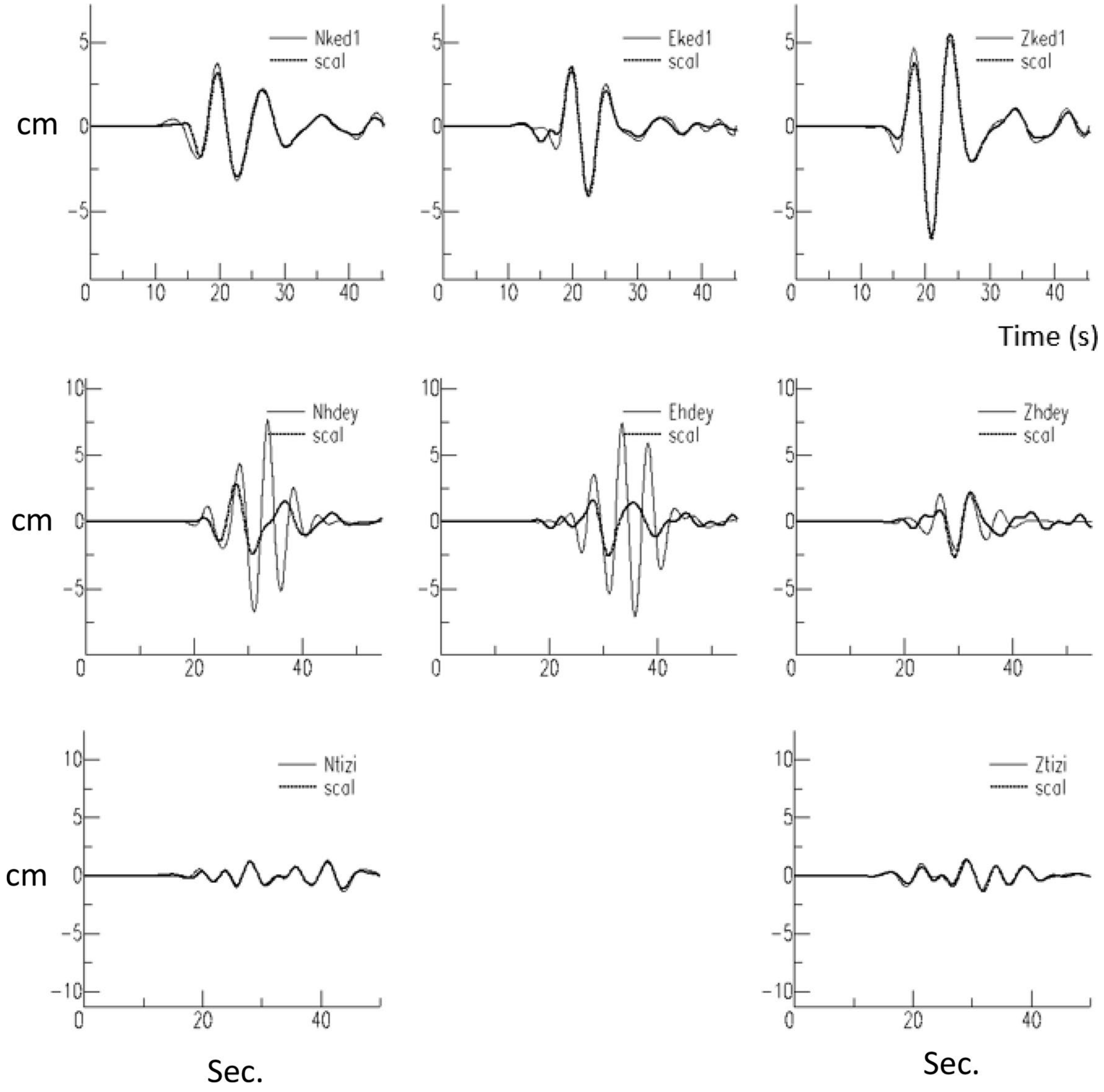

Fig. 19 same as Fig. 9 but without station HDEY to which a zero weight is attributed

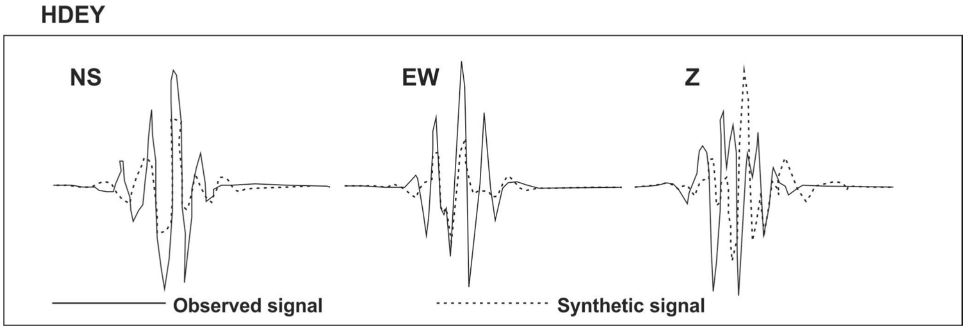

Fig. 20 Digitizing of Fig. 3 of Semmane et al.(2005) showing the modeling of the HDEY station that they obtained. Continuous line is the observed seismogram and dashed line the computed one. Note that modeling shows a high degree of misfit, as shown in our Figs. 6 and 19, but not as in our Fig. 9. NS is north–south component, EW is a east–west component and Z is a vertical component.Y-axis in cm and X-axis time in seconde

Table 3 Root Mean Square misfit function (RMS) and seismic moment (Mo) in for the different inversions as presented in this study. TELE: teleseismic; SM: strong motion; SAR: InSAR; CU: coastal uplift

	1seg model	2seg model	2seg model without HDEY	4seg model
RMS TELE	0.486	0.475	0.509	0.456
RMS SM	0.515	0.216	0.199	0.220
RMS SAR	0.087	0.079	0.081	0.080
RMS GPS	0.181	0.115	0.106	0.108
RMS CU	0.181	0.167	0.167	0.167
Mo (dyn.cm)	2.96×10^{26}	3.67×10^{26}	3.15×10^{26}	3.73×10^{26}

The inversion of the synthetic SAR data recovers logically slip zones a1 and a5located in the area where most of the SAR data points are located, while the a2, a3 and a4 slip zones are located in areas with too few SAR points exist. The shape of the asperities a1 and a5 is approximately found, showing a spreading tendency.

Finally, the joint inversion of all the synthetic datasets together provides the overall best result, retrieving all the five slip zones, although with less resolved properties for the extreme ones, a3 and a4, with respect to a1, a2, and a5.

2.13 4seg model

In this section, we present only result obtained from joint inversion of all set of data for the 4seg model. The results of individual inversions of the 2seg and 4seg models present many similarities, for this we judge not necessary to show them again.

The synthetic slip model is characterized now by nine slip patches: a1 to a5 is the same as for the 2seg model, and a6 to a9 is located on the offshore flat and ramp segments (Figs. 21 and 23. Slip amplitude on a6 to a9 is relatively smaller because we do not expect a high slip value on these offshore segments. As expected, for slip patches a1 to a5, the joint inversion provides a result similar to that obtained with the 2seg model (Fig. 25).

Slip zones a6 and a7 on the flat segment are hardly retrieved, weaker than the synthetic ones. Nothing is found on the farthest ramp segment (a8 and a9). In fact, low values of slip (<0.1 m) can be found on the ramp segment, but cannot be considered as significant.

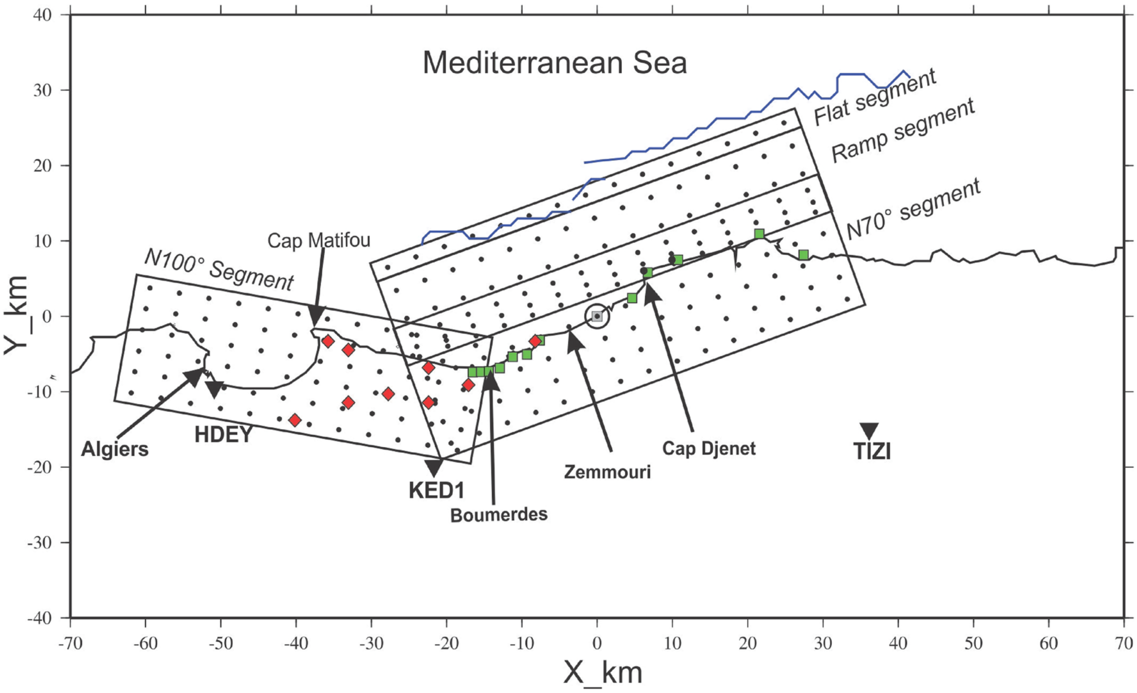

Fig. 21 Surface projection of model 4seg. For the other elements, same caption as Fig. 3

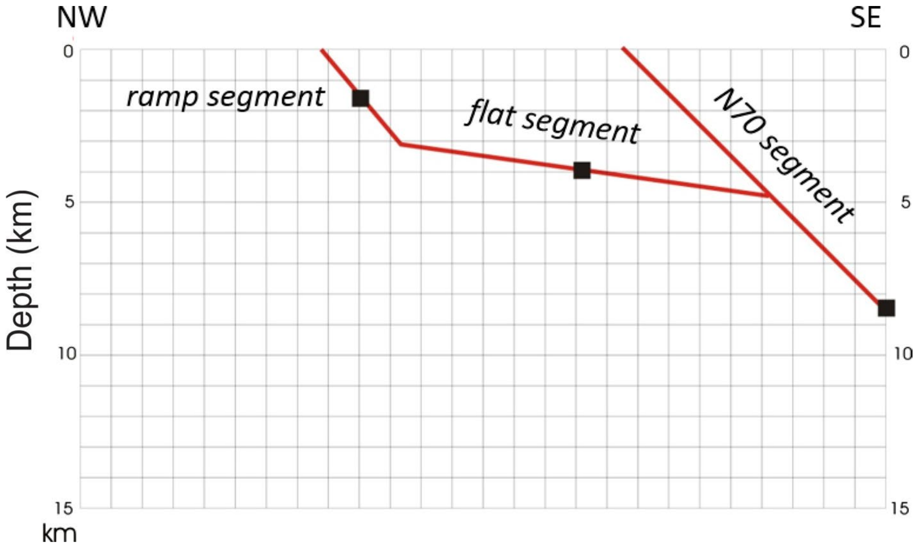

Fig. 22 Vertical cross section perpendicular to azimuth N70, showing the position of the three fault segments oriented N70°, called the N70° (main) segment, ramp segment, and flat segment. Black squares are located at the middle of each segment

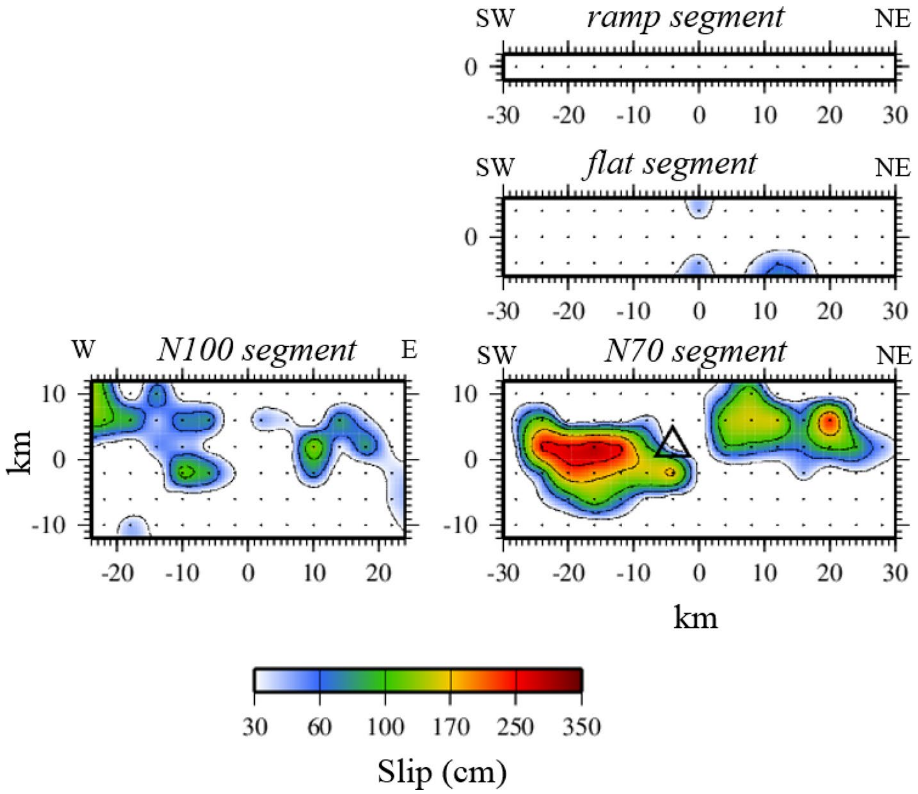

Fig. 23 Slip distribution from the joint inversion of all datasets with 4seg model.For other elements, same caption as Fig. 4

3 Discussion–Conclusion

We started by using a simple model with uniform geometry (strike N70°, dip 40°), identical to the one used in Delouis et al. (2004) except for the dip value, which was formerly 45°, but by incorporating, InSAR and strong motion data. Our simple model provided a slip distribution similar to the one of Delouis et al. (2004), but we identified some incompatibility among the more complete datasets, with difficulty in modeling the records of the SM station HDEY and the GPS data. This led us to explore more complexity in the geometry of the rupture model.

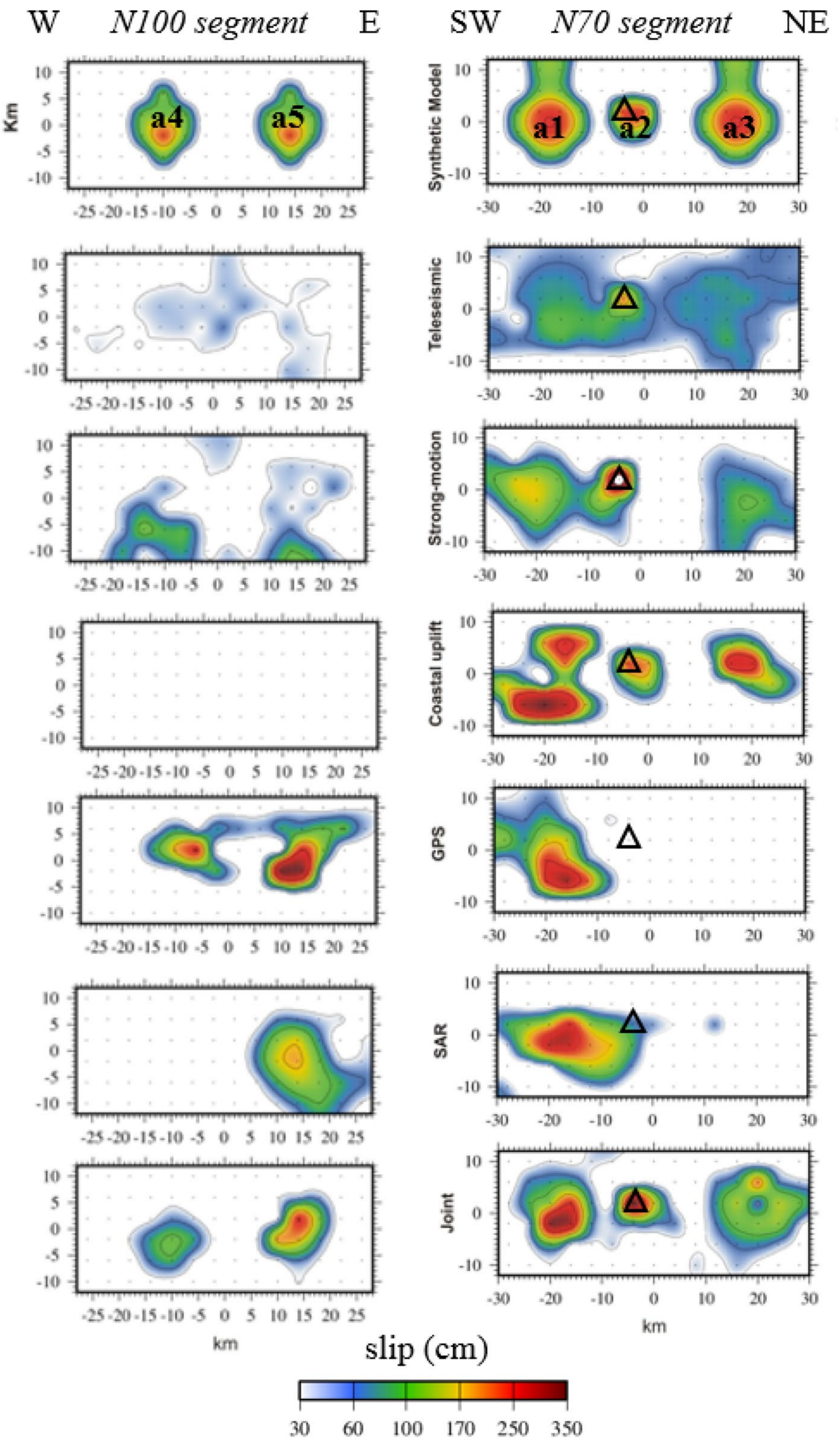

Fig. 24 Resolution tests with synthetic data for the 2seg model. Left column: N70° segment; right column: N100° segment. The first row displays the synthetic model. Rows 2 to 6 show the results of the inversions for individual datasets, teleseismic, strong motion, coastal uplift, GPS, and InSAR, respectively. The last row displays the result of the joint inversion of all the datasets together. For other elements, same caption as Fig. 4

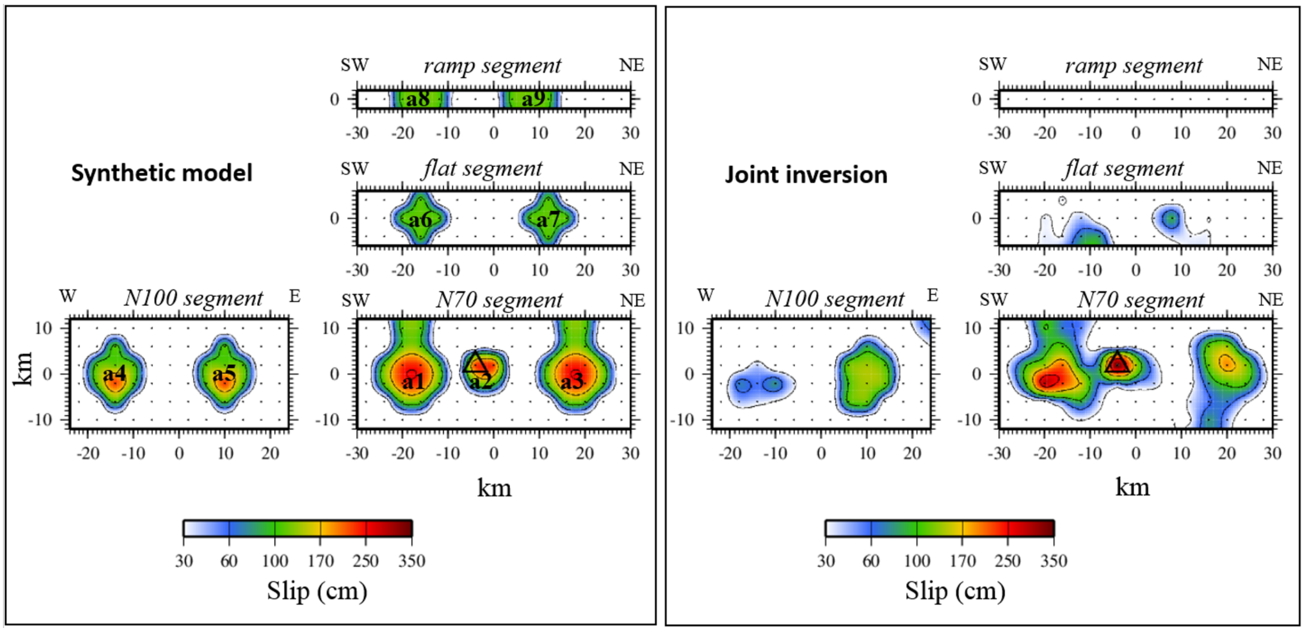

Fig. 25 Resolution tests with synthetic data for the 4seg model. Left frame: synthetic model; right frame: result of the joint inversion of all datasets. For other elements, same caption as Fig. 4

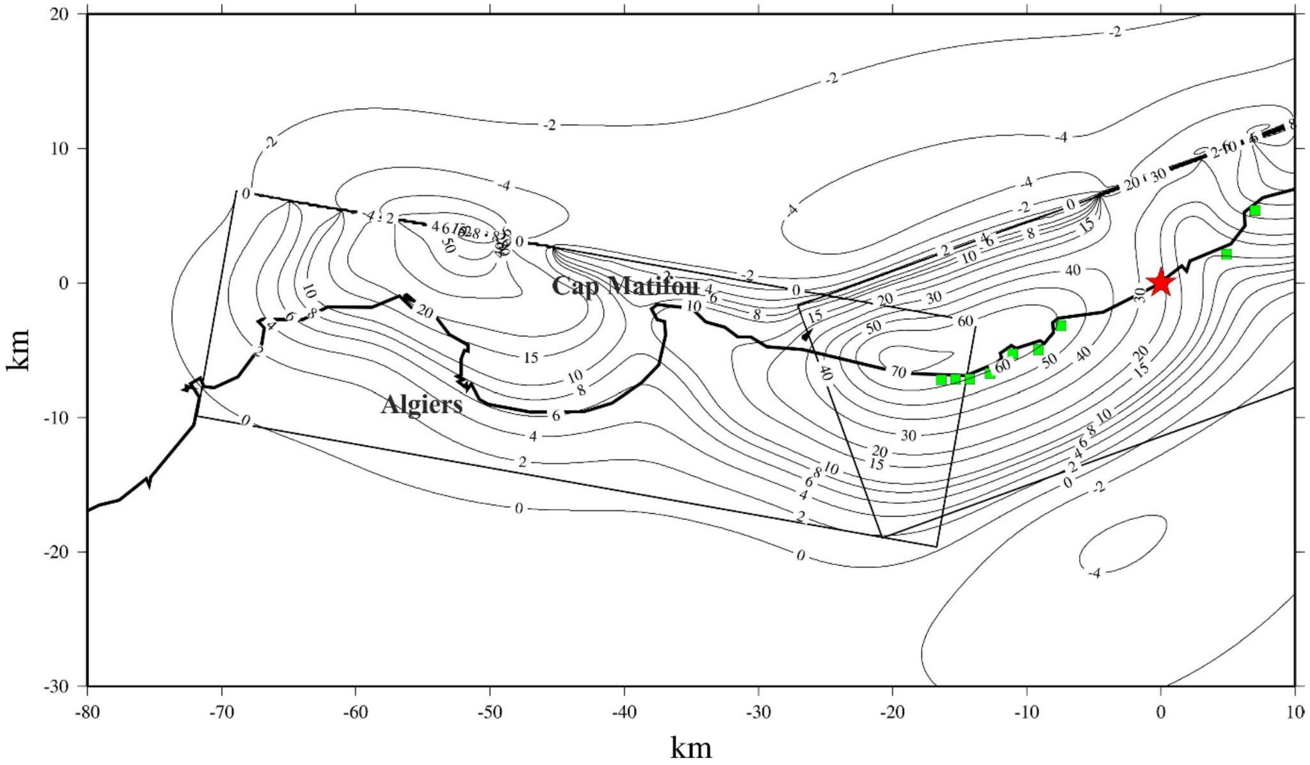

Fig. 26 Vertical displacement at the surface produced by the slip distribution found with the 2seg model (Fig. 17), from the joint inversion of all the datasets. Heavy black line represents the coastline; thin black curves represent the vertical displacement with values indicated in cm; red star represents the mainshock epicenter; rectangular frames represent the surface projection of the contours of the fault segments of the 2seg model; green squares represent the points where the coastal uplift was measured. Vertical axis is defined as positive towards the North, horizontal axis is defined as positive towards the east

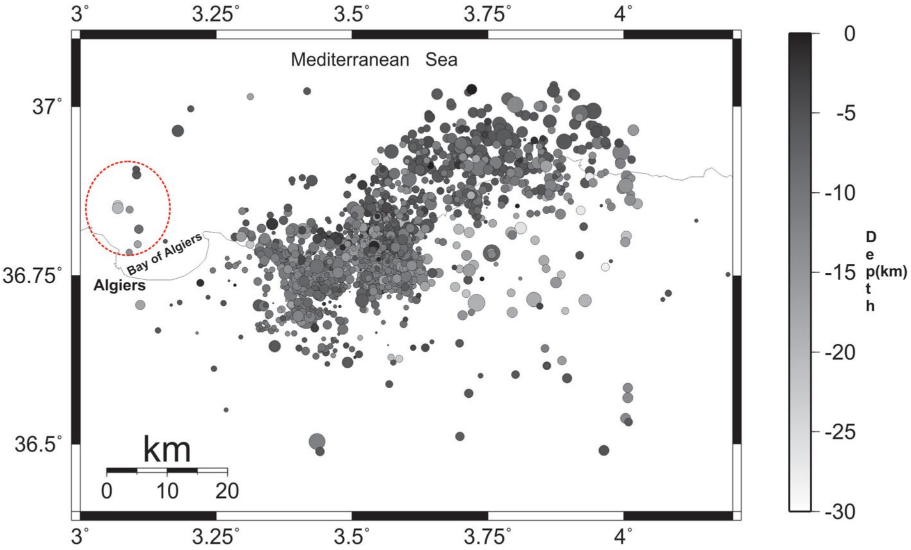

Fig. 27 Aftershocks of the 2003 Boumerdes earthquake from May 23 to June 30, 2003, modified from Fig. 3 of Kherroubi et al. (2017). Red circle zone: area of aftershocks in the immediate vicinity of the westernmost slip zone of our preferred 2seg model

A change in the strike of the western part of the fault had been already proposed by Belabbes et al. (2009), and the activation of the shallow offshore ramp and flat faults had been suggested by Deverchère et al. (2005). Based on these elements, we constructed two alternative models, 2seg and 4seg, incorporating a second segment oriented N100° (2seg model) in the west and two additional segments offshore (4seg model).

With the 2seg model, the apparent incompatibility among the datasets could be solved with a slip distribution modeling correctly all the datasets, particularly the GPS and SM station HDEY, which were problematic. However, a new slip area appears offshore Algiers (Fig. 9), not identified in previous studies.

In our sense, this new area may represent a shallow after-slip rather than a purely coseismic slip.

We showed that this slip zone is required by the SM station HDEY only. We also emphasize that the other data (TELE, GPS, INSAR, CU), although globally little impacted by this slip zone, are compatible (RMS values in Table 3). For example, we observe that computed InSAR fringes (Fig. 14) are effectively nearly closing at, or just east of, Cap Matifou, as do the observed ones. Regarding coastal uplift, nothing was documented in the Algiers area. In order to assess whether this westernmost slip zone should have produced coastal uplift, which should have been observed, we calculated the related vertical uplift along the coast near Algiers (Fig. 26). We find the predicted uplift to be equal to or lower than 0.20 m in the Algiers area, a value that may be effectively below the observational threshold.

From synthetic tests, we learn that we must be careful in not over-interpreting the precise shape of this westernmost slip zone, which is not very well resolved.

The distribution of aftershocks of Boumerdes-Zemmouri earthquake shows that the events are mainly located in the vicinity of the N70 fault segment, with very few events west of Cap Matifou. At first glance, aftershocks do not support the existence of the westernmost slip area as we found offshore Algiers. However, the temporary seismic network installed to record the aftershocks sequence was deployed essentially east of Cap Matifou, and it did not cover the entire area of Algiers, especially offshore. Also, the temporary seismic network did not record an aftershocks series with a magnitude <4 in this area. Based on the data from the international catalogues (e.g. USGS), we can nonetheless state that no aftershocks with $M>4$ occurred in this area.

Nonetheless, a few aftershocks located by Ouyed et al. (2011), and to a lesser extent by Kherroubi et al. (2017), may be correlated with the westernmost slip zone, as shown in Fig. 27.

Intensity maps of the 2003 mainshock do not show any localized increase of the intensity in the western part of Algiers that may be related to our westernmost slip zone. One possibility to explain this, but unproved at this time, would be that the offshore coseismic rupture corresponding to the western part of the N100 segment of our 2seg model generated few destructive high frequencies, i.e. was characterized by the emission of low-frequency seismic waves. This could be related to a relatively slow (< 1–2 km/s) propagating rupture, but the limited available near-source seismological records do not allow to resolve this.

Regarding the coseismic activation of the offshore faults derived from the observations of Deverchère et al. (2005), our inversion result with model 4seg suggests that some slip with multi-decimeter amplitude may have occurred there, especially on the flat segment. However, from the synthetic tests, we confirm that resolution on the offshore segments is low, and we conclude that the inland data, even completed by the teleseismic records, are insufficient to resolve moderate amplitude slip. Hence, the question of the coseismic activation of shallow offshore secondary faults remains open.

Acknowledgements We would like to express our special thanks to Nasser Laouami (CGS) and Mustapha Méghraoui (EOST) for providing us with strong motion and uplifts data.

References

Ayadi A, Dorbath C, Ousadou F, Maouche S, Chikh M, Bounif MA, Meghraoui M (2008) Zemmouri earthquake rupture zone (Mw 6.8, Algeria): Aftershocks sequence relocation and 3D velocity model. J Geophys Res 113:B09301. https://doi.org/10.1029/2007JB005257

Belabbès S, Wicks C, Cakir Z, Meghraoui M (2009) Rupture parameters of the 2003 Zemmouri (Mw 6.8), Algeria, earthquake from joint inversion of interferometric synthetic aperture radar, coastal uplift, and GPS. J Geophys Res 114:B03406. https://doi.org/10.1029/2008JB005912,2009

Bouchon M (1981) A simple method to calculate Green's functions for elastic layered media. Bull Seism Soc Am 71:959–971

Bounif A, Dorbath C, Ayadi A, Meghraoui M, Beldjoudi H, Laouami N, Frogneux M, Slimani A, Alasset PJ, Kharroubi A, Ousadou F, Chikh M, Harbi A, Larbes S, Maouche S (2004) The 21 May 2003 Zemmouri (Algeria) earthquake Mw = 6.8: relocation and aftershocks sequence analysis. Geophys Res Lett 31:L19606. https://doi.org/10.1029/2004GL020586

Cetin E, Meghraoui M, Cakir Z, Akoglu AM, Mimouni O, Chebbah M (2012) Seven years of postseismic deformation following the 2003 Mw = 6.8 Zemmouri earthquake (Algeria) from InSAR time series. Geophys Res Lett 39:10307. https://doi.org/10.1029/2012GL051344

Corona C, Marchesi M, Martini C, Ridella C (1987) Minimizing multimodal Functions of continuous variables with the simulated annealing algorithm. ACM Trans Math Software 13:262–280

Delouis B, Giardini D, Lundgren P, Salichon J (2002) Joint inversion of InSAR, GPS, teleseismic and strong motion data for the spatial and temporal distribution of earthquake slip: Application to the 1999 Izmit mainshock. Bull Seismol Soc Am 92:278–299

Delouis B, Vallée M, Meghraoui M, Calais E, Maouche S, Lammali K, Mahsas A, Briole P, Benhamouda F, Yelles-Chaouche A (2004) Slip distribution of the 2003 Boumerdes-Zemmouri earthquake, Algeria, from teleseismic, GPS, and coastal uplift data. Geophys Res Lett 31:L18607. https://doi.org/10.1029/2004GL020687

Déverchère J, Yelles K, Domzig A, Mercier de Lépinay B, Bouillin JP, Gaullier V, Bracène R, Calais E, Savoye B, Kherroubi A, Le Roy P, Pauc H, Dan G (2005) Active thrust faulting offshore Boumerdes, Algeria, and its relations to the 2003 Mw 6.9 earthquake. Geophys Res Lett 32:L04311. https://doi.org/10.1029/2004GL021646

Kherroubi A, Yelles-Chaouche A, Koulakov I, Déverchère J, Beldjoudi H, Haned A, Semmane FA, C, (2017) Full aftershock sequence of the Mw 69 2003 Boumerdes earthquake. Space-time distribution, local tomography and seismotectonic implications, Algeria. https://doi.org/10.1007/s00024-017-1571-5

Mahsas A, Lammali K, Yelles-ChaoucheA CE, Freed AM, Briole P (2008) Shallow afterslip following the 2003 May 21, Mw = 6.9 Boumerdes earthquake, Algeria. Geophys J Int 172:155–166

Meghraoui M, Maouche S, Chemaa B, Cakir Z, Aoudia A, Harbi A, Alasset PJ, Ayadi A, Bouhadad Y, Benhamouda F (2004) Coastal uplift and thrust faulting associated with the Mw = 6.8 Zemmouri (Algeria) earthquake of 21 May, 2003. Geophys Res Lett 31:L19605. https://doi.org/10.1029/2004GL020466

Nabelek J (1984). Determination of earthquake fault parameters from inversion of body waves. PhD thesis, MI T, Cambridge University

Ouyed M, Idres M, Bourmatte A, Boughacha MS, Samai S, Yelles-Chaouche A, Haned A, Aidi C (2011) Attempt to identify seismic sources in the eastern Mitidja basin using gravity data and aftershock sequence of the Boumerdes (May 21, 2003; Algeria) earthquake. J Seismol 15:173–189. https://doi.org/10.1007/s10950-010-9218-3

Savage JC (1980) Dislocations in seismology. Navarro FRN. Dislocations in Solids edn. North-Holland, New York, pp 252–339

Semmane F, Campillo M, Cotton F (2005) Fault location and source process of the Boumerdes, Algeria, earthquake inferred from geodetic and strong motion data. Geophys Res Lett 32:L01305. https://doi.org/10.1029/2004GL021268

Yelles K, Lammali K, Mahsas A, Calais E, Briole P (2004) Coseismic deformation of the May 21st, 2003, Mw = 6.8 Boumerdes earthquake, Algeria, from GPS measurements. Geophys Res Lett 31:L13610. https://doi.org/10.1029/2004GL019884